Applied Energy 331 (2023) 120448

Contents lists available at ScienceDirect

Applied Energy

journal homepage: www.elsevier.com/locate/apenergy

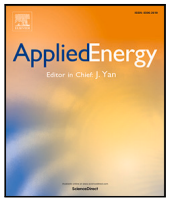

Effective estimation of the state-of-charge of latent heat thermal energy storage for heating and cooling systems using non-linear state observers

Hector Bastida *, Ivan De la Cruz-Loredo, Carlos E. Ugalde-Loo

School of Engineering, Cardiff University, Queen's Buildings, The Parade, Cardiff, CF24 3AA, Wales, UK

ARTICLE INFO

Keywords:
Latent heat thermal energy storage
State-of-charge
Non-linear observer
One-dimensional dynamic model
Cooling
Heating

ABSTRACT

An effective quantification of the energy absorbed and supplied by latent heat thermal energy storage (LHTES) units is critical to maximise their use within thermal systems. An effective control of the charging and discharging processes of these units demands an accurate estimation of the state-of-charge (SoC). However, a direct and reliable SoC estimation requires incorporating internal sensors to monitor the temperature gradient of the phase change material (i.e. the storage medium), resulting in higher instrumentation costs and technical specifications. These issues may be relieved by adopting state observers for SoC estimation to drastically reduce the number of measurements. This paper bridges this gap by presenting a novel and direct method for estimating the SoC of LHTES units, both for heating and cooling applications, based on a non-linear state observer. The observer is based on a simple one-dimensional dynamic model of the thermal store and the thermophysical properties of the storage medium and the heat transfer fluid, which are usually provided by manufacturers. This enables the estimation of the internal temperatures of the LHTES unit and, in turn, SoC calculation. The observer implementation is simple as it requires three measurements only as input variables (i.e. the mass flow rate and the input and output temperatures of the heat transfer fluid). The SoC estimation approach is assessed through dynamic simulations of two LHTES units: one for a heating application and one for a cooling application. The results show that the SoC can be estimated with root mean square and mean absolute errors of less than 4.6% and 3.62%, respectively, compared with experimental measurements.

1. Introduction

Thermal energy storage (TES) considers a range of technologies capable of storing thermal energy, enabling the energy stored to be used at a later stage when required. This is achieved by modifying the enthalpy of the storage medium by heating or cooling it. A thermal store is used to act as a buffer between supply and demand schedules. Making an analogy with electricity networks, a TES unit operates essentially as a thermal battery. Depending on the specific TES technology, the thermal energy can be used within hours, days or even months later, and deployed into industrial processes, an individual household, buildings, a district network, or perhaps a community, either for heating and cooling applications or for power generation. For instance, water tanks are widely used in households for domestic hot water provision [1], while in a district cooling system, ice tanks may be adopted [2]. A thermal store can be also used as a buffer tank to avoid the short cycling of a heat pump in a heating system [3].

TES systems may play a critical role in decarbonising the building and industrial sectors [4–6]. The operational flexibility afforded by incorporating TES devices into thermal systems enables the efficient management of energy supply and demand through the implementation of load shaping techniques (e.g. peak demand, load shifting, valley filling) [7,8]. In turn, this flexibility also allows for the use of low-carbon technologies, such as heat pumps [9,10], the adoption of intermittent renewable energy sources [11] including solar collector systems [12] and concentrated solar power [13], and the integration of different energy vectors — bringing substantial economic and environmental benefits. For instance, a TES plant may be used to facilitate the optimal integration of solar energy into heating systems and reduce their operational cost [14]. In the same vein, the feasibility of adopting TES systems in buildings has been assessed in [15] for a wide variety of technologies.

The adoption of TES units requires implementing effective control strategies to regulate their operation. For instance, model predictive control has been employed to analyse the optimal charging period of thermal stores while reducing operational costs and achieving thermal comfort [16,17]. On the other hand, optimisation algorithms have been

* Corresponding author.
E-mail addresses: BastidaHernandezJH@cardiff.ac.uk (H. Bastida), DeLaCruzLoredoI@cardiff.ac.uk (I. De la Cruz-Loredo), Ugalde-LooC@cardiff.ac.uk (C.E. Ugalde-Loo).

https://doi.org/10.1016/j.apenergy.2022.120448
Received 17 August 2022; Received in revised form 9 November 2022; Accepted 27 November 2022
Available online 9 December 2022

Nomenclature

Abbreviations

1-D	One-dimensional
2-D	Two-dimensional
HTF	Heat transfer fluid
LHTES	Latent heat thermal energy storage
ODE	Ordinary differential equation
PCM	Phase change material
PDF	Probability density function
SHTES	Sensible heat thermal energy storage
SoC	State-of-charge
TES	Thermal energy storage

Greek symbols

β	Correction factor for U
γ	Shape parameter for a PDF
Δh_l	Specific latent heat [J/kg]
η	Location parameter for a PDF
θ	Scale parameter for a PDF
μ	Mean
μ_f	Dynamic viscosity [Ns/m^2]
ρ	Density [kg/m^3]
σ	Standard deviation
φ	Probability density function

Variables

A	Area [m^2]
c_p	Specific heat [J/(kg°C)]
D_t	Hydraulic diameter [m]
E	Energy [J, Wh]
e	Estimation error vector
h	Enthalpy [J/kg]
k	Thermal conductivity [W/(m°C)]
m	Mass [kg]
$\dot{m}_f$	Mass flow rate [kg/s]
N	Number of nodes
Nu	Nusselt number
Pr	Prandtl number
P	Power [W]
q	Heat transfer rate [J/s]
r	Radius [m]
Re	Reynolds number
T	Temperature [°C]
U	Overall heat transfer coefficient [W/(m^2°C)]
u	Input vector
V	Volume [m^3]
v_f	Mean velocity of the HTF [m/s]
x	State vector
y	Output vector

Subscripts

a	Ice TES tank tube 1
b	Ice TES tank tube 2
ex	Refers to external surface
exp	Experimental
f	Refers to heat transfer fluid
i	Node index for temperature
in	Input
k	Node index for state
l	Latent heat
ls	Refers to losses at heat transfer coefficient
o	Output
obs	Observed
p	Refers to phase change material
s	Sensible heat
sim	Simulated
T	Total
tr	Refers to transfer
w	Water in the ice TES tank

Superscripts

G	Refers to Gumbel minimum PDF
L	Refers to Lognormal PDF
W	Refers to Weibull PDF

implemented to achieve an optimal operation of the TES units [18,19]. Nevertheless, these analyses do not consider key variables such as temperatures and mass flow rates. Therefore, to guarantee their performance during charging and discharging processes, automatic controllers must be designed considering the thermal-hydraulic dynamics of the TES units and the type of sensors available for monitoring the state-of-charge (SoC). For instance, hot water tanks, which use the sensible heat of water to store thermal energy, can be effectively charged or discharged by monitoring the temperature gradient of the water within the tank. To this end, temperature sensors are mounted through the tank's height. The SoC is then estimated using the temperature measurements and the specific heat capacity of water [20].

Unlike sensible heat TES (SHTES) units, latent heat TES (LHTES) devices store thermal energy using a heat transfer fluid (HTF) and the heat capacity of a storage medium, termed phase change material (PCM). A PCM is a substance that releases or absorbs a large amount of energy during its phase transition, which takes place at a nearly constant temperature [21,22]. These materials have a wide range of applications, including solar cookers [23], transport refrigeration vehicles [24], wallboards to store solar heat in buildings [25], thermocrete walls (concrete modification with PCM incorporation) [26], and ceiling boards for active cooling in refurbished buildings [27], to name only but a few. Solid–liquid PCM is the most suitable storage medium to be used for an LHTES unit [4]. Compared to SHTES units, the substantially larger energy density per unit of mass of the storage medium [28,29] makes LHTES units an often-employed technology to support the efficient management of thermal systems. However, effectively monitoring the temperature gradient in a PCM is arguably costly and challenging. The phase change causes the total volume of the PCM to temporarily fractionate into liquid and solid volumes irregularly distributed in the unit. Thus, reliable and accurate temperature measurements are only achieved when several sensors are installed [21,30].

Methods for determining the temperature gradient in a PCM using a reduced number of temperature sensors have been presented in the literature [31]. However, their limited accuracy results in significant SoC estimation errors. Instead, other methods for indirectly determining the SoC have been developed. For instance, pressure sensors may be used to estimate the SoC by establishing a relation between the pressure changes and the change in the phase fraction of a PCM [32]. For ice tanks where the PCM is water, an often-used approach is based on the difference in density between the liquid and frozen water. A differential pressure transducer is employed to measure the change in volume when ice is formed. Although the method is simple and highly accurate (with

a reported 2% accuracy of the full scale of the sensor), the amount of ice may be over or understated due to the presence of air pockets or compression effects [33]. The interested reader is referred to [31] for a detailed analysis of all these methods, including advantages and drawbacks.

To circumvent the costly implementation of internal temperature sensors, a concept borrowed from modern control theory may be adopted for the management of TES units [20,34,35]: the state observer (also called state estimator). An observer is a computer-implemented dynamic system used to estimate the internal state of the system under study from measurements of its inputs and outputs [36]. Thus, it can estimate the temperature gradient in a PCM using only the input and output temperature and flow rate measurements of the HTF circulated through the storage unit. The use of observers has been analysed mainly for electrical energy storage systems [37–39], with limited application in thermal stores. Ref. [20] is relevant though, where an observer is used to estimate the internal temperature of a hot water tank (i.e. a SHTES system).

An observer to estimate the temperature distribution of an LHTES unit requires a mathematical model of the thermal store which accurately reproduces its dynamic behaviour. For instance, one-dimensional (1-D) and two-dimensional (2-D) models of TES units have been presented in [40,41]. Their modelling approach is based on the energy balance and spatial discretisation of the unit's volume into a finite number of volumes or nodes (also called control volumes). A set of ordinary differential equations (ODEs) describes the behaviour of the temperatures of the HTF and PCM in each node. This approach is suitable for observer design, as the temperatures fully describe the internal state of the system. Then, the SoC can be calculated using the estimated values of all PCM nodes.

A pioneering work using state estimation was presented in [35], where a Kalman filter and a spatially discretised 2-D model of an LHTES unit are used. Here, the SoC is defined as the mean liquid phase fraction of the PCM, which is a function of the internal temperature of the storage unit. SoC calculation requires the solution of 12 partial differential equations, which are simplified to a set of low-order non-linear ODEs using spatial discretisation. Although the phase fraction describes accurately the energy released or absorbed during phase change, an integral of the function representing this process needs to be evaluated, which substantially increases the computation time. To incur less computational effort, the specific enthalpy of the PCM can be used instead to describe the thermal dynamics as it has a direct relation with energy balance [40,42]. Ref. [31] follows this approach, where the SoC is calculated using the specific enthalpy of the phase transition of the PCM; however, the results obtained have limited accuracy.

To the best of the authors' knowledge, the use of state observers to estimate the SoC of an LHTES unit which considers the whole temperature range of the storage medium within the unit is restricted to [35,43]. Despite their good accuracy, these observers are based on extended Kalman filters, which involve a highly complex design process. In other words, simple non-computationally demanding methods are yet to be developed to estimate the internal temperature of LHTES units to, in turn, enable SoC calculation with a reduced number of sensors.

To bridge the aforementioned research gap, this paper presents a methodology for obtaining the SoC of practical LHTES units for heating and cooling applications. The approach employs a simple non-linear observer to accurately estimate the temperatures of the PCM and the HTF. As the observer is based on a 1-D spatially discretised model of the thermal store defined by a set of ODEs, this has a significantly simpler structure than the observer models reported in [35,43], which are based on 2-D models.

Experimentally verified models available in the public literature have been adopted for observer design. The LHTES unit model reported in [42] is used for the heating application, while the model of an ice TES tank in [40] is used for the cooling application. The SoC is calculated using the temperatures estimated by the observers and the specific enthalpy curve of the PCM (obtained from the characterisation of the specific heat curve) and implemented as a look-up table. This is important as it reduces the computation time compared to integration-based approaches such as those in [35]. The SoC estimation method was verified using the data reported in [41], where the total stored energy and the SoC are provided.

The main contributions of this paper are summarised as follows:

- The design and implementation of a non-linear observer to estimate the internal temperature gradient of the PCM and the HTF in LHTES units.
- A method to calculate the SoC of LHTES units based on the outputs of the observer and the characterisation of the specific heat curve of the PCM.
- The verification of the SoC calculation method using simple 1-D dynamic models of LHTES units available in the open literature (and which have been experimentally validated).

2. Description and modelling approach of LHTES units

The dynamic modelling approach used in this paper is dictated by the internal structure of the LHTES unit. Different structures for commercial units are available. For instance, the PCM can be encapsulated in containers with different shapes, such as spheres, cylinders, or slabs, with a HTF flowing through the space between the capsules to charge or discharge the unit. However, tube arrangements submerged into the PCM may be adopted to enable the flow of the HTF [44]. Metallic fins within the PCM may be incorporated to enhance the heat transfer between the HTF and the PCM [41].

The thermal stores for heating and cooling applications adopted in this paper possess an internal structure of non-encapsulated PCM with submerged HTF tubes — with relevant parameters and properties provided in Appendix B. Fig. 1 shows a shell and tube TES unit for heating applications. The shell is filled with a high-density polyethylene PCM (Rigidex HD6070EA) [45]. This PCM exhibits an enthalpy hysteresis, where the melting temperatures for charging (120 °C) and discharging (135 °C) are different. A high-performance synthetic organic transfer medium is used as the HTF, which flows through 72 parallel tubes within the thermal store. The dynamic model of the TES unit was obtained following a 1-D modelling approach. Further details on the mathematical model are available in [42] for the interested reader.

For cooling applications, an ice TES tank manufactured by Calmac was adopted. The ICEBANK 1098 tank model uses water as the PCM, harvesting ice to store cooling. The internal tube arrangement is shown in Fig. 2 and consists of 34 spiralled tube pairs made of polyethylene. A mixture of water and glycol at 34% is used as the HTF. The dynamic 1-D model of the ice TES tank is available in [40]. In the reference, model verification was conducted by comparing experimental results reported in [46,47] with simulation results obtained with the model.

The 1-D models reported in [40,42] constitute the basis for the observer designs presented in Section 3 of this paper. The rationale behind the choice of these rather different units is to demonstrate the capabilities and simplicity of the developed methodology, to explore its adaptability to different internal geometries and different types of PCM, and to show the feasibility of the use of non-linear observers to estimate internal temperatures, without the use of additional sensors, to enable SoC calculation for both a hot and a cold store. For completeness, the modelling approach in these references is briefly explained next.

2.1. Dynamic modelling

The heat transfer occurring during charging and discharging of the LHTES units is described in [40,42], where the energy balance between the HTF and the PCM is assessed and the overall heat transfer coefficient is calculated. Equal hydraulic and temperature conditions

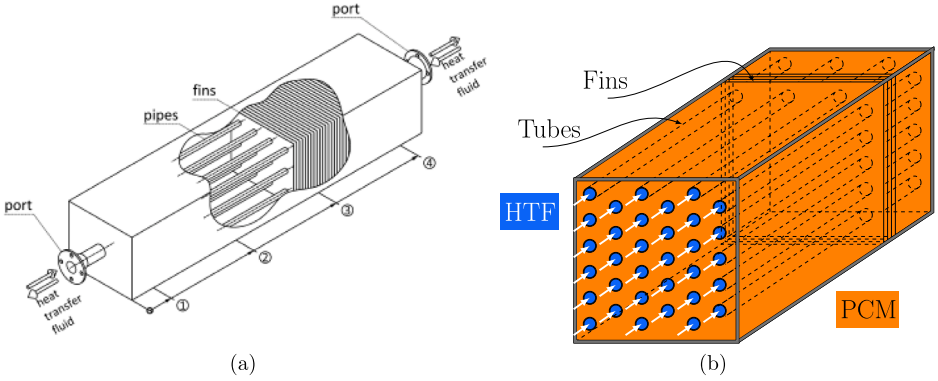

Fig. 1. Shell and tube TES unit: (a) Design sketch [41] and (b) schematic [42].

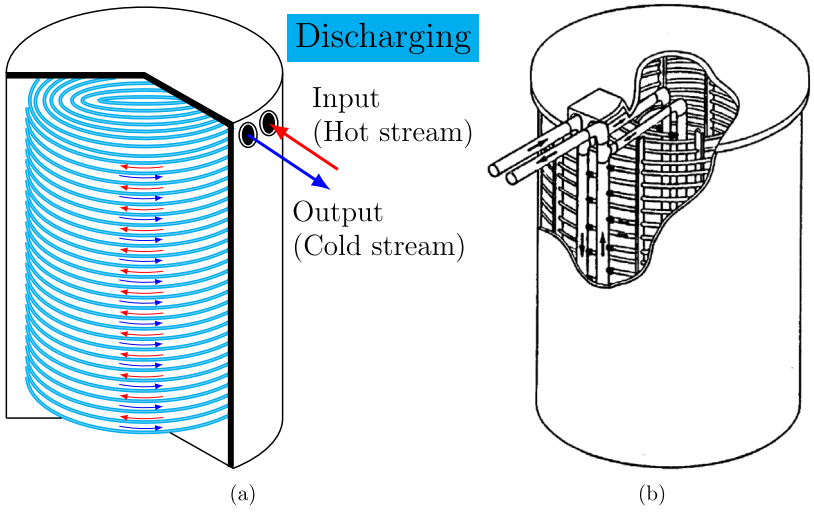

Fig. 2. (a) Internal geometry of an ice TES tank showing the direction of the HTF in each level [40]. (b) Location of the two external and two internal headers [48].

are assumed for all the tubes in the TES units. Thus, the analysis done over a single tube in the shell and tube TES unit and for a pair of tubes in the ice TES tank is considered as representative of the behaviour of all tubes. In both cases, the tanks are assumed to be well-insulated and, thus, heat losses are assumed negligible.

To apply energy balance it is necessary to define a control volume. Fig. 3 shows the lateral and frontal cross-sectional views of a single internal tube with the boundaries of a control volume. This includes the HTF inside the tube flowing at a certain temperature $T_{f,in}$ [°C] and mass flow rate $\dot{m}_f$ [kg/s], the PCM enclosing it, and the wall of the tube. The size of the control volume is defined by Δx through the length of the tube L [m]. Thus, the rate of change of the energy stored by the HTF ($\dot{E}_f$ [W]) and the PCM ($\dot{E}_p$ [W]) is defined as

$$\dot{E}_f = q_{in} + U A_{tr} \left(T_p - T_f\right), \tag{1}$$

$$\dot{E}_p = U A_{tr} \left(T_f - T_p\right), \tag{2}$$

where q_{in} [J/s] is the heat injected by the HTF crossing the tube, U [W/(m^2°C)] is the overall heat transfer coefficient, A_{tr} [m^2] is the heat transfer area, T [°C] denotes temperature, and subscripts 'f' and 'p' stand for HTF and PCM. Further details on the derivation of (1) and (2) can be found in Appendix A for the interested reader.

The heat transfer produced by the forced convection between the HTF and the internal wall of the tube, and conduction in the radial direction into the tube and the PCM are included in the calculation of U. The reader is referred to [42] for further details. On the other hand, the ice TES tank model presented in [40] includes two tubes within the control volume. Thus, three heat transfer coefficients are considered: between the HTF and PCM, between the PCM volumes around the tubes, and between the PCM volume that achieves the phase change and the PCM volume that stays at 0 °C.

Note: The calculation of U is carried out dynamically for both the model of the LHTES unit and the observer, which are discussed in Section 3. This means that changes in the mass flow rate and the temperature of the HTF are considered by this calculation. In addition, the values of the thermophysical properties of the HTF, which are temperature dependent, are updated according to the value of the temperature of the HTF at any given time. Additional details on the calculation of U are provided in Appendix C.

The last stage of the modelling approach is to discretise the volume of the tubes into N nodes (or discrete volumes). The discretisation over a single tube of the shell and tube TES unit is schematically shown in Fig. 4. For the ice TES tank, for clarity, the discretisation process is schematically shown in Fig. 5(a) for a single spiralled tube out of the tube pair. However, to simplify the modelling, these tubes (denoted 'a' and 'b') are assumed unrolled [40]. This is shown in Fig. 5(b), with the discretisation of the two unrolled tubes shown in Fig. 5(c). Therefore, the energy balance described by (1) and (2) is established for each node of a single tube of the shell and tube unit and tubes 'a' and 'b' of the ice TES tank. Each node thus includes two ODEs for the model of the shell and tube TES unit and four ODEs for the model of the ice TES tank. The corresponding total number of equations is, respectively, $2N$ and $4N$.

The modelling approach used in [40]–[42] simplifies the mathematical representation of an LHTES unit by assuming an equal internal

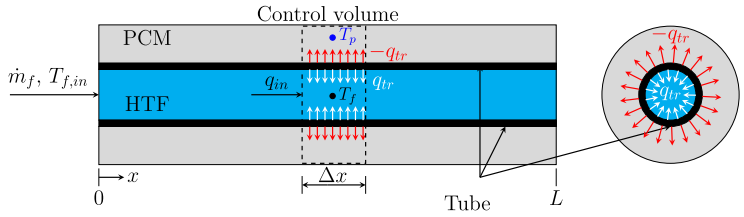

Fig. 3. Lateral (left) and cross-sectional (right) view of a tube inside an LHTES unit with the definition of control volume. White and red arrows show the radial direction of the heat flow between the HTF and the PCM. For a heat flow from the PCM to the HTF, which implies a higher PCM temperature, the white arrows illustrate the heat transferred to the HTF. Conversely, for a higher HTF temperature, the red arrows denote the heat transferred to the PCM. The sign convention is adopted based on the energy balance of the HTF volume.

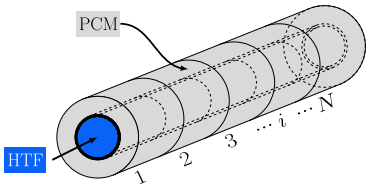

Fig. 4. Single tube split into N nodes.

flow and an equal temperature distribution for all tubes throughout the tank. Thus, the energy balance implementation for a single tube in the shell and tube TES unit and for two tubes in the ice TES tank is representative of the dynamic behaviour for all tubes (i.e. 72 tubes in total for the shell and tube TES unit and 34 pairs of enrolled tubes for the ice tank). Accurate simulation results are reported in the three references following this approach.

2.2. On the differences between the two TES configurations

Although both TES units employ a similar internal structure (i.e. tubes submerged into a PCM), the material of the tubes is substantially different and the tubes are arranged in a different way. The ice tank has pairs of spiralled tubes made of polyethylene, while the shell and tube TES unit has straight tubes made of the carbon alloy steel P235GH. In addition to impacting the number of differential equations representing the heat transfer between the HTF and the PCM (i.e. the ice tank considers twice as many equations compared to the shell and tube TES unit if the same number of nodes is used for the discretisation process), the tube arrangement has an effect in the overall heat transfer coefficient. For both units, heat losses were not considered. However, for modelling simplicity of the ice tank, the tubes were assumed unrolled. Although these assumptions simplify the calculation of the overall heat transfer coefficient, an error is caused. This has been minimised by using a correction factor defined through a fitting process of the simulation results with the available experimental data. (For further information on the calculation of the heat transfer coefficient, the reader is referred to Appendix C.)

The PCM being employed is another important difference in the TES units under study, where water is used for the ice tank and polyethylene RigidexHD6070EA for the shell and tube unit. In addition, a mixture of water–glycol at 34% is employed as the HTF for the ice tank, whereas for the shell and tube TES unit this is the synthetic organic heat transfer medium Marlotherm SH [49].

3. Description of the observer

Since the TES models adopted in this paper exhibit a high non-linearity arising from the temperature dependence of the thermophysical properties of the PCM and the HTF, such as specific heat and density, non-linear observers are required to estimate the internal temperatures.

3.1. Observer design

Using state–space notation, the models of the LHTES units are described in compact form by

$$\begin{aligned} \dot{T} = \dot{\mathbf{x}} &= f(\mathbf{x}, \mathbf{u}), \\ \mathbf{y} &= j(x), \end{aligned} \tag{3}$$

where $\mathbf{u}$, $\mathbf{x}$ and $\mathbf{y}$ are the input, state, and output vectors, $\dot{\mathbf{x}} = f(\mathbf{x}, \mathbf{u})$ is the set of non-linear ODEs of the dynamic model, and $j(x)$ is the scalar system output, which is the output temperature of the HTF. Given the different number of tubes used to formulate the models of the two TES units adopted in this paper, the design of their respective observer is explained separately.

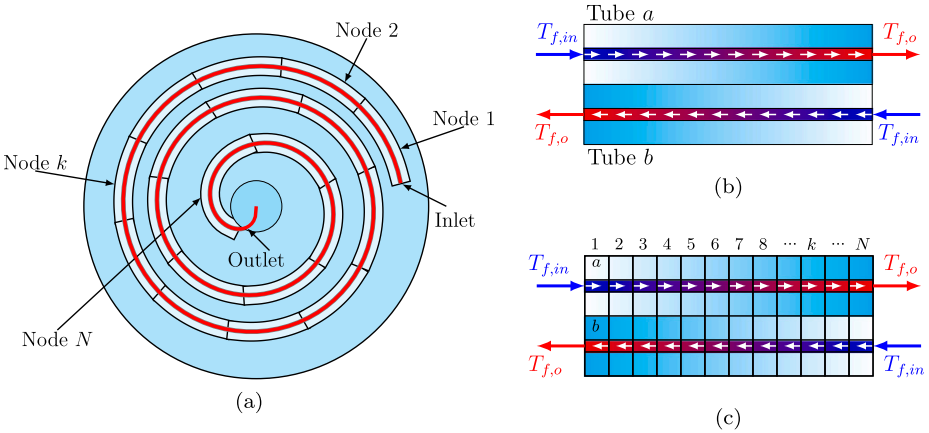

Fig. 5. Tube arrangement for an ice TES tank (figures reproduced from [40]). (a) Single tube tank split into N nodes. (b) Unrolled tubes with the counter flow directions of the fluid and the ice growing in the first nodes for tube 'a' and the last note for tube 'b' (the white shading depicts ice formation). (c) Control volumes of both tubes.

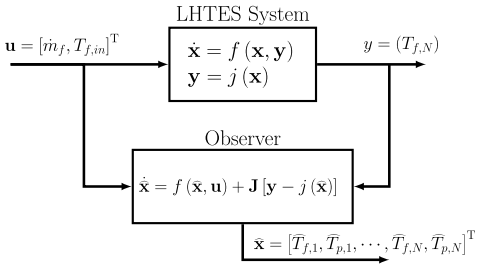

Fig. 6. Implementation of the non-linear state observer for the shell and tube TES unit.

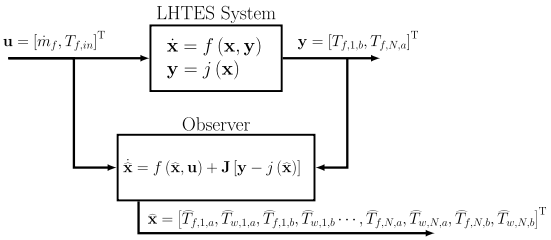

Fig. 7. Implementation of the non-linear state observer for the ice TES tank.

Note: In non-linear control theory, variable **h** is commonly used to define the output vector of a system. To avoid confusion with the notation for specific enthalpy (h) and specific latent heat (Δh_l), variable **j** is adopted instead to denote a vector of system outputs (and j for a single output).

The observer structure is defined as [36]

$$\dot{\hat{\mathbf{x}}} = f\left(\hat{\mathbf{x}}, \mathbf{u}\right) + \mathbf{J}\left(\mathbf{y} - j\left(\hat{x}\right)\right), \tag{4}$$

where $\hat{\mathbf{x}}$ is the estimated state vector and **J** is a diagonal matrix of constant coefficients. **J** must be designed to ensure the estimation error for all states converges to zero ($\tilde{\mathbf{e}} = \mathbf{x} - \hat{\mathbf{x}} = 0$). The observer is defined using the same differential equations (i.e. $f(\mathbf{x}, \mathbf{u})$) of the system model.

3.1.1. Design for the shell and tube TES unit

Using the notation adopted in [42], **x**, **u** and **y** are defined as

$$\mathbf{x} = \left[T_{f,1}\ T_{p,1}\ T_{f,2}\ T_{p,2}\ \cdots\ T_{f,N}\ T_{p,N}\right]^{T}, \tag{5}$$

$$\mathbf{u} = \left[\dot{m}_f\ T_{f,in}\right]^{T}, \tag{6}$$

$$\mathbf{y} = T_{f,o} = T_{f,N}, \tag{7}$$

where $\dot{m}_f$ [kg/s] is the mass flow rate of the HTF (water), $T_{f,in}$ [°C] is the temperature of the HTF at the inlet of the tube and $T_{f,o}$ [°C] at the outlet of the tube, $T_{f,i}$ [°C] is the temperature of the HTF in the ith node, and $T_{p,i}$ [°C] is the temperature of the PCM in the ith node (see Fig. 4). A schematic for the observer implementation is shown in Fig. 6.

The design of **J** requires analysing the observability of the system. This is challenging considering the high non-linearity of the system. However, positive entries of **J** guarantee the estimation error converges to zero. For the shell and tube TES unit, the state observer is described by (8) given in Box I, where c_p [J/(kg°C)] is the specific heat, N is the number of nodes, ρ [kg/m^3] is the density, and V [m^3] is the volume in each node. Details on the derivation of (8) have been provided in Appendix D. The diagonal elements of $\mathbf{J}\left(J_1, J_2, \cdots, J_N\right)$ in (4), explicitly appearing in (8), were heuristically defined as 0.1. The specific heat was characterised using probability density functions (PDFs), with details given in Appendix E. All parameters related to the thermophysical properties of the HTF and the PCM are provided in Appendix B.

3.1.2. Design for the ice TES tank

The model of the ice TES tank considers a pair of tubes forming a counter-flow heat exchanger. This is representative of the 34 counter-flow heat exchangers formed by all the spiralled pairs of tubes (68 tubes in total), as shown in [40]. The notation in [40] for the temperatures of the nodes is used, where subscripts 'f' and 'w' stand respectively for the HTF and the PCM (in this case water), and subscripts 'a' and 'b' are used to distinguish between each tube. Since energy balance is applied for each pair of tubes, four states are included in each node when the system is discretised and, thus, the total number of states is $4N$. Using state–space notation, **x** is defined by

$$\mathbf{x} = \left[T_{f,1,a}\ T_{w,1,a}\ T_{f,1,b}\ T_{w,1,b}\ \cdots\ T_{f,N,a}\ T_{w,N,a}\ T_{f,N,b}\ T_{w,N,b}\right]^{T}. \tag{9}$$

As the mass flow rate of the HTF is assumed to be evenly distributed in both tubes, only two variables are included in **u**:

$$\mathbf{u} = \left[\dot{m}_f\ T_{f,in}\right]^{T}, \tag{10}$$

where $T_{f,in}$ is the input temperature of the HTF and $\dot{m}_f$ is the total mass flow rate of the HTF entering the tank divided by the total number of tubes.

The internal tank configuration gives rise to two system outputs, which are the temperatures of the HTF at the opposite ends of the tubes, and the observer must consider both (although in the real system both HTFs merge through the system headers to form a single output [40]). The inlet of tube 'a' and the outlet of tube 'b' are located in node 1. Conversely, the outlet of tube 'a' and the inlet of tube 'b' are located in node N. Thus, **y** is defined as

$$\mathbf{y} = \left[T_{f,1,b}\ T_{f,N,a}\right]^{T}. \tag{11}$$

Fig. 7 shows a schematic of the observer. Based on the mathematical model of the tank and the definition of **x**, **u**, and **y**, the observer is described by (12) given in Box II, where index k is equal to $4(i-1)+1\ \forall\ i \in \{1, 2, \ldots, N\}$, U is the overall heat transfer coefficient between the HTF and water, U_w is the heat transfer coefficient between the control volumes of water of both tubes, and U_{ls} is the heat transfer coefficient between the portion of water with the phase change completed and the portion remaining at 0 °C [40]. As in the design for the shell and tube unit, **J** was here obtained heuristically and its diagonal elements were set as 0.5. Derivation of (12) follows a similar procedure as that for (8), which is provided in Appendix D.

3.2. Observer implementation

The observers were implemented in MATLAB/Simulink. Charging and discharging processes of the TES units were simulated to assess the observer performance under different operating conditions.

3.2.1. Observer performance for the shell and tube TES unit

The operating conditions reported in [41] were used. These include the input temperature profile of the HTF ($T_{f,in}$) for charging and discharging and a constant mass flow rate of 1.02 kg/s for both processes. The PDFs used in the calculation of the specific heat have been adapted from a Weibull distribution for charging and a Lognormal distribution for discharging [41], and are provided in Appendix E. The TES model and the non-linear observer were each discretised into 20 nodes, which was deemed sufficient to achieve accurate simulation results without incurring significant computation time [42].

Fig. 8 shows the responses of the observer for the simulation of the charging process. The temperatures of the HTF and PCM for node i are given by the system states $T_{f,i} = x_{2i-1}$ and $T_{p,i} = x_{2i}$. For clarity, only the temperatures in nodes 1, 11 and 20 are provided, namely $T_{f,1} = x_1$, $T_{p,1} = x_2$, $T_{f,11} = x_{21}$, $T_{p,11} = x_{22}$, $T_{f,20} = x_{39}$, $T_{p,20} = x_{40}$. The initial

$$\begin{bmatrix} \dot{\hat{T}}_{f,1} \\ \dot{\hat{T}}_{p,1} \\ \vdots \\ \dot{\hat{T}}_{f,i} \\ \dot{\hat{T}}_{p,i} \\ \vdots \\ \dot{\hat{T}}_{f,N} \\ \dot{\hat{T}}_{p,N} \end{bmatrix} = \begin{bmatrix} \dot{\hat{x}}_1 \\ \dot{\hat{x}}_2 \\ \vdots \\ \dot{\hat{x}}_k \\ \dot{\hat{x}}_{k+1} \\ \vdots \\ \dot{\hat{x}}_{2N-1} \\ \dot{\hat{x}}_{2N} \end{bmatrix} = \begin{bmatrix} \left[\frac{\dot{m}_f c_{p,f,1}(T_{f,in}-\hat{x}_1)+U(A_{tr}/N)(\hat{x}_2-\hat{x}_1)}{\rho_{f,1}c_{p,f,1}(V_f/N)}\right] + \left[J_1\left(x_{2N-1}-\hat{x}_{2N-1}\right)\right] \\ \left[\frac{U(A_{tr}/N)(\hat{x}_1-\hat{x}_2)}{\rho_{p,2}c_{p,p,2}(V_p/N)}\right] + \left[J_2\left(x_{2N-1}-\hat{x}_{2N-1}\right)\right] \\ \vdots \\ \left[\frac{\dot{m}_f c_{p,f,k}(\hat{x}_{k-2}-\hat{x}_k)+U(A_{tr}/N)(\hat{x}_{k+1}-\hat{x}_k)}{\rho_{f,k}c_{p,f,k}(V_f/N)}\right] + \left[J_k\left(x_{2N-1}-\hat{x}_{2N-1}\right)\right] \\ \left[\frac{U(A_{tr}/N)(\hat{x}_k-\hat{x}_{k+1})}{\rho_{p,k+1}c_{p,p,k+1}(V_p/N)}\right] + \left[J_{k+1}\left(x_{2N-1}-\hat{x}_{2N-1}\right)\right] \\ \vdots \\ \left[\frac{\dot{m}_f c_{p,f,N-1}(\hat{x}_{2N-3}-\hat{x}_{2N-1})+U(A_{tr}/N)(\hat{x}_{2N}-\hat{x}_{2N-1})}{\rho_{f,2N-1}c_{p,f,2N-1}(V_f/N)}\right] + \left[J_{2N-1}\left(x_{2N-1}-\hat{x}_{2N-1}\right)\right] \\ \left[\frac{U(A_{tr}/N)(\hat{x}_{2N-1}-\hat{x}_{2N})}{\rho_{p,2N}c_{p,p,2N}(V_p/N)}\right] + \left[J_N\left(x_{2N-1}-\hat{x}_{2N-1}\right)\right] \end{bmatrix}. \tag{8}$$

Box I.

$$\begin{bmatrix} \dot{\hat{T}}_{f,1,a} \\ \dot{\hat{T}}_{w,1,a} \\ \dot{\hat{T}}_{f,1,b} \\ \dot{\hat{T}}_{w,1,b} \\ \vdots \\ \dot{\hat{T}}_{f,i,a} \\ \dot{\hat{T}}_{w,i,a} \\ \dot{\hat{T}}_{f,i,b} \\ \dot{\hat{T}}_{w,i,b} \\ \vdots \\ \dot{\hat{T}}_{f,N,a} \\ \dot{\hat{T}}_{w,N,a} \\ \dot{\hat{T}}_{f,N,b} \\ \dot{\hat{T}}_{w,N,b} \end{bmatrix} = \begin{bmatrix} \dot{\hat{x}}_1 \\ \dot{\hat{x}}_2 \\ \dot{\hat{x}}_3 \\ \dot{\hat{x}}_4 \\ \vdots \\ \dot{\hat{x}}_k \\ \dot{\hat{x}}_{k+1} \\ \dot{\hat{x}}_{k+2} \\ \dot{\hat{x}}_{k+3} \\ \vdots \\ \dot{\hat{x}}_{4N-3} \\ \dot{\hat{x}}_{4N-2} \\ \dot{\hat{x}}_{4N-1} \\ \dot{\hat{x}}_{4N} \end{bmatrix} = \begin{bmatrix} \left[\frac{\dot{m}_f c_{p,f,1}(T_{f,in}-\hat{x}_1)+U(A_{tr}/N)(\hat{x}_2-\hat{x}_1)}{\rho_{f,1}c_{p,f,1}(V_f/N)}\right] + \left[J_1 e_a + J_1 e_b\right] \\ \left[\frac{U(A_{tr}/N)(\hat{x}_1-\hat{x}_2)+U_w(A_{ex}/N)(\hat{x}_4-\hat{x}_2)+U_{ls}(A_{ex}/N)(0-\hat{x}_2)}{\rho_{w,2}c_{p,w,2}(V_w/N)}\right] + \left[J_2 e_a + J_2 e_b\right] \\ \left[\frac{\dot{m}_f c_{p,f,3}(\hat{x}_7-\hat{x}_3)+U(A_{tr}/N)(\hat{x}_4-\hat{x}_3)}{\rho_{f,3}c_{p,f,3}(V_f/N)}\right] + \left[J_3 e_a + J_3 e_b\right] \\ \left[\frac{U(A_{tr}/N)(\hat{x}_3-\hat{x}_4)+U_w(A_{ex}/N)(\hat{x}_2-\hat{x}_4)+U_{ls}(A_{ex}/N)(0-\hat{x}_4)}{\rho_{w,4}c_{p,w,4}(V_w/N)}\right] + \left[J_4 e_a + J_4 e_b\right] \\ \vdots \\ \left[\frac{\dot{m}_f c_{p,f,k}(\hat{x}_{k-4}-\hat{x}_k)+U(A_{tr}/N)(\hat{x}_{k+1}-\hat{x}_k)}{\rho_{f,k}c_{p,f,k}(V_f/N)}\right] + \left[J_i e_a + J_i e_b\right] \\ \left[\frac{U(A_{tr}/N)(\hat{x}_k-\hat{x}_{k+1})+U_w(A_{ex}/N)(\hat{x}_{k+3}-\hat{x}_{k+1})+U_{ls}(A_{ex}/N)(0-\hat{x}_{k+1})}{\rho_{w,k+1}c_{p,w,k+1}(V_w/N)}\right] + \left[J_{i+1} e_a + J_{i+1} e_b\right] \\ \left[\frac{\dot{m}_f c_{p,f,k+2}(\hat{x}_{k+6}-\hat{x}_{k+2})+U(A_{tr}/N)(\hat{x}_{k+3}-\hat{x}_{k+2})}{\rho_{f,k+2}c_{p,f,k+2}(V_f/N)}\right] + \left[J_{i+2} e_a + J_{i+2} e_b\right] \\ \left[\frac{U(A_{tr}/N)(\hat{x}_{k+2}-\hat{x}_{k+3})+U_w(A_{ex}/N)(\hat{x}_{k+1}-\hat{x}_{k+3})+U_{ls}(A_{ex}/N)(0-\hat{x}_{k+3})}{\rho_{w,k+3}c_{p,w,k+3}(V_w/N)}\right] + \left[J_{i+3} e_a + J_{i+3} e_b\right] \\ \vdots \\ \left[\frac{\dot{m}_f c_{p,f,4N-3}(\hat{x}_{4N-7}-\hat{x}_{4N-3})+U(A_{tr}/N)(\hat{x}_{4N-2}-\hat{x}_{4N-3})}{\rho_{f,4N-3}c_{p,f,4N-3}(V_f/N)}\right] + \left[J_{N-3} e_a + J_{N-3} e_b\right] \\ \left[\frac{U(A_{tr}/N)(\hat{x}_{4N-3}-\hat{x}_{4N-2})+U_w(A_{ex}/N)(\hat{x}_{4N}-\hat{x}_{4N-2})+U_{ls}(A_{ex}/N)(0-\hat{x}_{4N-2})}{\rho_{w,4N-2}c_{p,w,4N-2}(V_w/N)}\right] + \left[J_{N-2} e_a + J_{N-2} e_b\right] \\ \left[\frac{\dot{m}_f c_{p,f,4N-1}(T_{f,in}-\hat{x}_{4N-1})+U(A_{tr}/N)(\hat{x}_{4N}-\hat{x}_{4N-1})}{\rho_{f,4N-1}c_{p,f,4N-1}(V_f/N)}\right] + \left[J_{N-1} e_a + J_{N-1} e_b\right] \\ \left[\frac{U(A_{tr}/N)(\hat{x}_{4N-1}-\hat{x}_{4N})+U_w(A_{ex}/N)(\hat{x}_{4N-2}-\hat{x}_{4N})+U_{ls}(A_{ex}/N)(0-\hat{x}_{4N})}{\rho_{w,4N}c_{p,w,4N}(V_w/N)}\right] + \left[J_N e_a + J_N e_b\right] \end{bmatrix}. \tag{12}$$

Box II.

conditions of the observer states were set to 50 °C. Fig. 8(a) shows the input and output temperatures of the HTF ($T_{f,in}$ and $T_{f,o}$). It can be seen from Fig. 8(b) that the observer (solid traces, $\hat{x}_1$, $\hat{x}_2$, $\hat{x}_{21}$, $\hat{x}_{22}$, $\hat{x}_{39}$, $\hat{x}_{40}$) is able to track the system states accurately (dashed traces, x_1, x_2, x_{21}, x_{22}, x_{39}, x_{40}). The HTF temperatures (i.e. x_1, x_{21}, x_{39}) show small oscillations at the beginning of the process for about 1 min. The PCM temperatures (i.e. x_2, x_{22}, x_{40}) present a slightly slower response as highlighted in the zoomed-in graph.

To further assess the performance of the observer, the plots of the estimation error for all states are shown in Figs. 8(c) and 8(d). The error converges to zero in about 1 min for the temperatures of the HTF (see Fig. 8(c)) and in approximately 5 min for the temperatures of the PCM (Fig. 8(d)). These convergence times are deemed acceptable considering the slow dynamics exhibited by TES units [21].

The estimation errors for the temperatures of the HTF exhibit a behaviour that changes with the node location. For the nodes closer to the HTF inlet, the error converges to zero faster than for those closer to the HTF outlet. On the other hand, a slower but more homogeneous response is presented for the error of the PCM temperatures.

Fig. 9 shows the temperature of nodes 1, 11 and 20 during discharging. Although all initial temperature conditions of the observer were established uniformly at 50 °C, about 100 °C less than the initial

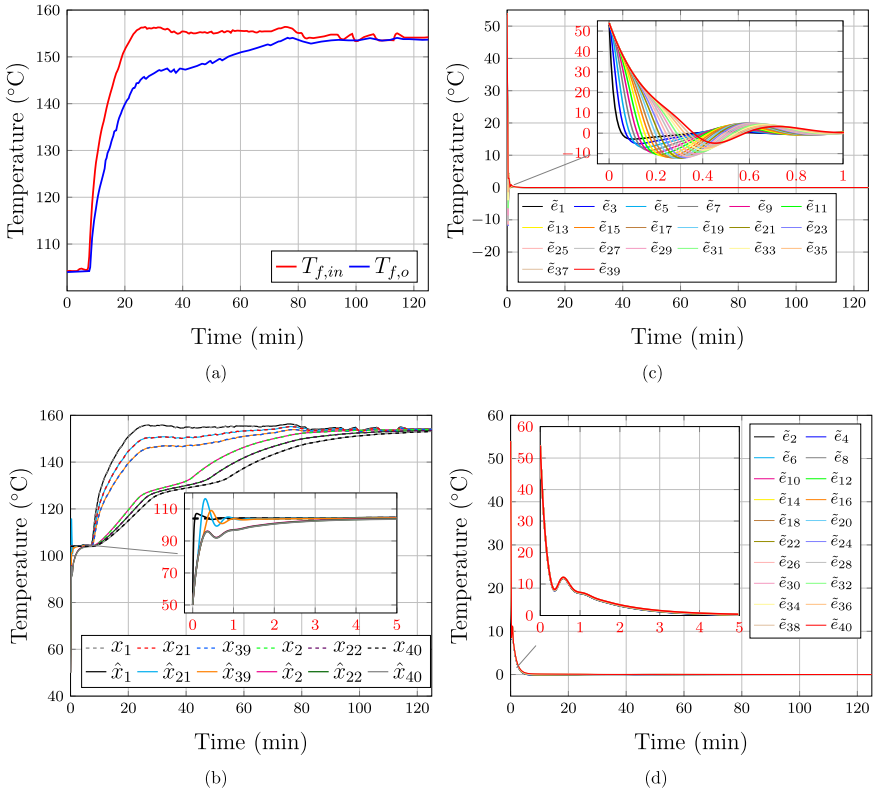

Fig. 8. Performance of the observer for the shell and tube TES unit during the charging process. (a) Input and output temperatures of the HTF. (b) States of the system and its observer (HTF and PCM temperatures are shown for nodes 1, 11, and 20). Estimation errors for the node temperatures of the (c) HTF and (d) PCM.

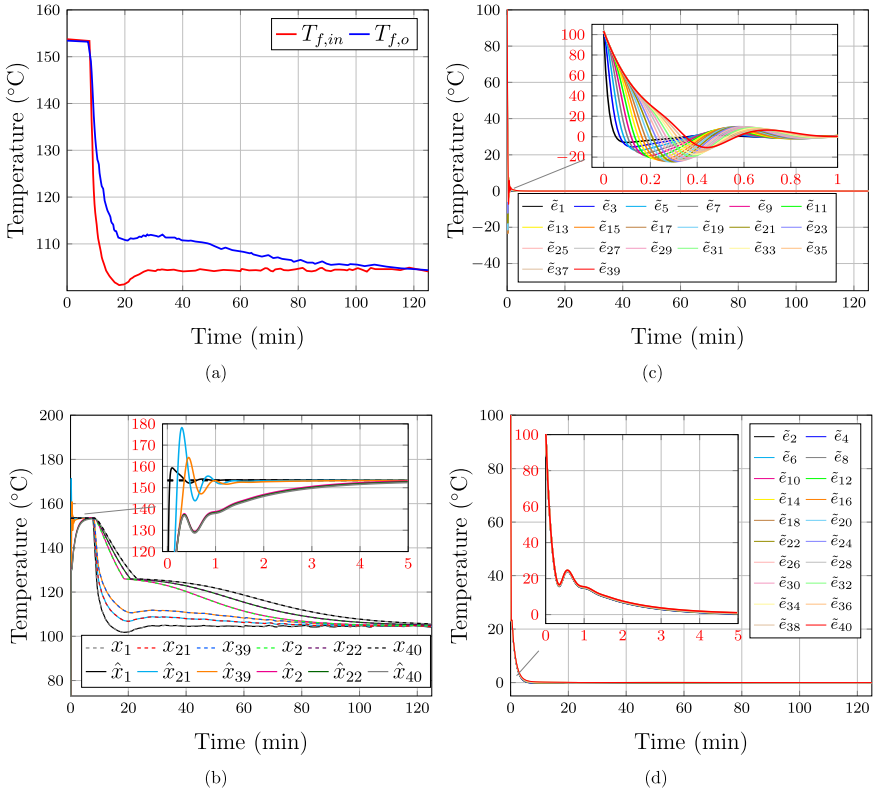

Fig. 9. Performance of the observer for the shell and tube TES unit during the discharging process: (a) Input and output temperatures of the HTF. (b) States of the system and its observer (HTF and PCM temperatures are shown for nodes 1, 11, and 20). Estimation errors for the node temperatures of the (c) HTF and (d) PCM.

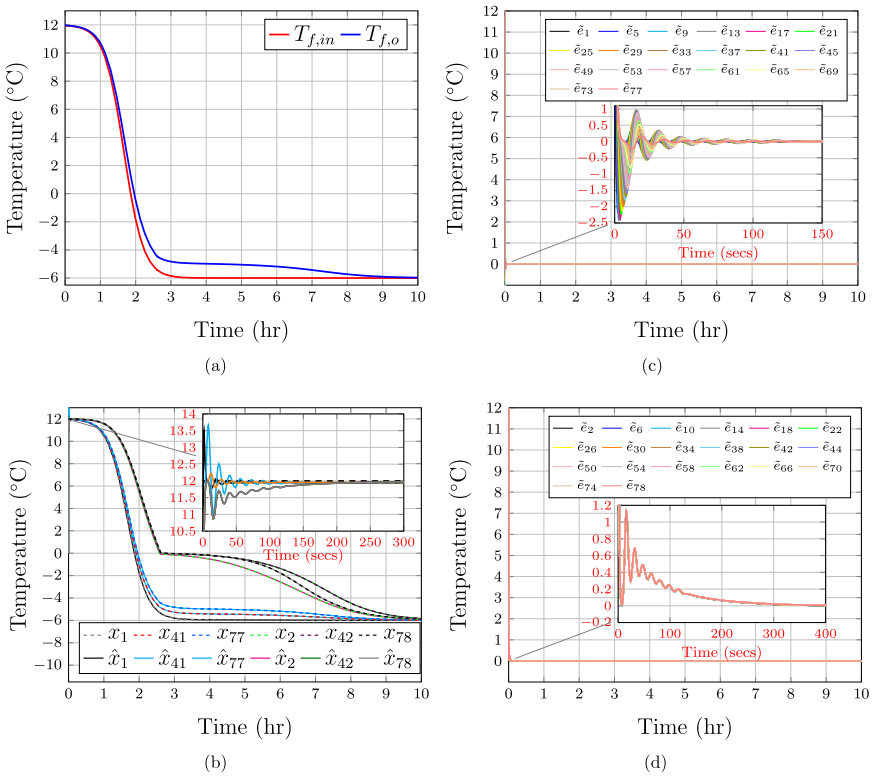

Fig. 10. Performance of the observer for the ice TES tank during the charging process. (a) Input and output temperatures of the HTF. (b) States of the system and its observer (HTF and PCM temperatures are shown for nodes 1, 11, and 20). Estimation errors for the node temperatures of the (c) HTF and (d) PCM.

conditions of the system reported in [41], the observer was able to reduce the estimation error to zero in 1 min for the HTF temperatures and in about 5 min for the PCM temperatures. It can be concluded that the observer has a comparable dynamic performance for charging and discharging even when the specific heat curve for each process is different.

3.2.2. Observer performance for the ice TES tank

The thermophysical properties of the HTF (glycol at 34%) are defined in [40] and reproduced in Appendix B, whereas the specific heat curve for the PCM (water) is provided in Appendix E. The initial temperature conditions of the observer were set to 0 °C. For clarity, only the temperatures and estimation errors for tube 'a' are plotted (i.e. numbers starting in 1 and 2, increasing in steps of 4, denoting the node temperatures of the HTF and the PCM, where subscript 'a' stands for tube 'a').

Fig. 10 shows the results for the charging process, where a constant mass flow rate of 20 kg/s was adopted and the input temperature of the HTF was reduced from 12 °C to −6 °C. According to the state–space representation in (12), the system states for tube 'a' are given by $T_{f,i,a} = x_{4i-3}$ and $T_{w,i,a} = x_{4i-2}$. Only the temperatures in nodes 1, 11 and 20 are provided, namely $T_{f,1,a} = x_1$, $T_{w,1,a} = x_2$, $T_{f,11,a} = x_{41}$, $T_{w,11,a} = x_{42}$, $T_{f,20,a} = x_{77}$ and $T_{w,20,a} = x_{78}$.

Fig. 10(a) shows the input and output temperatures of the HTF. The HTF and PCM actual and estimated temperatures (dashed traces and solid traces, respectively) are shown in Fig. 10(b), where it is evident that the observer successfully tracks the behaviour of the system. As shown in Fig. 10(c), the estimation error of the HTF temperatures converges to zero in less than 150 s, while for the PCM temperatures this occurs in around 300 s (see Fig. 10(d)).

Fig. 11 shows the simulation results for discharging. The estimation errors converge to zero in a similar timeframe as for charging, which is an acceptable performance given the slow dynamics of the ice TES tank.

4. SoC calculation method and its implementation

For simplicity and clarity in the explanation of the SoC calculation method, a normal PDF is adopted to describe the specific heat–temperature curve of a fictional PCM. Then, the implementation of the method is described and its suitability for spatially discretised dynamic models of LHTES units is discussed.

4.1. SoC calculation

The specific latent heat is the energy necessary per unit of mass to produce a change of phase in a PCM [28]. For instance, the specific latent heat to bring a mass of water at atmospheric pressure from liquid to solid and vice-versa is 334 kJ/kg [40]. During the phase change, the release or absorption of thermal energy occurs at a specific range of temperature. Thus, the storage capacity of an LHTES unit E_l [J] is calculated using the total mass of the PCM m [kg] and its specific latent heat Δh_l [J/kg] as

$$E_l = \Delta h_l m. \tag{13}$$

A specific enthalpy–temperature curve shows how the energy within a PCM suddenly increases or decreases during phase change [35]. Thus, it is possible to determine the internal energy of a storage unit at a particular PCM temperature. Let the specific enthalpy–temperature curve be defined by

$$h(T) = \int c_p(T)\, dT, \tag{14}$$

and the specific latent heat as

$$\Delta h_l = \int_{T_{\text{empty}}}^{T_{\text{full}}} c_p(T)\, dT, \tag{15}$$

where T_{empty} [°C] and T_{full} [°C] are the temperatures of the PCM that limit the transition zone between phases. The specific heat–temperature curve is obtained by differentiating (14), which is necessary as the

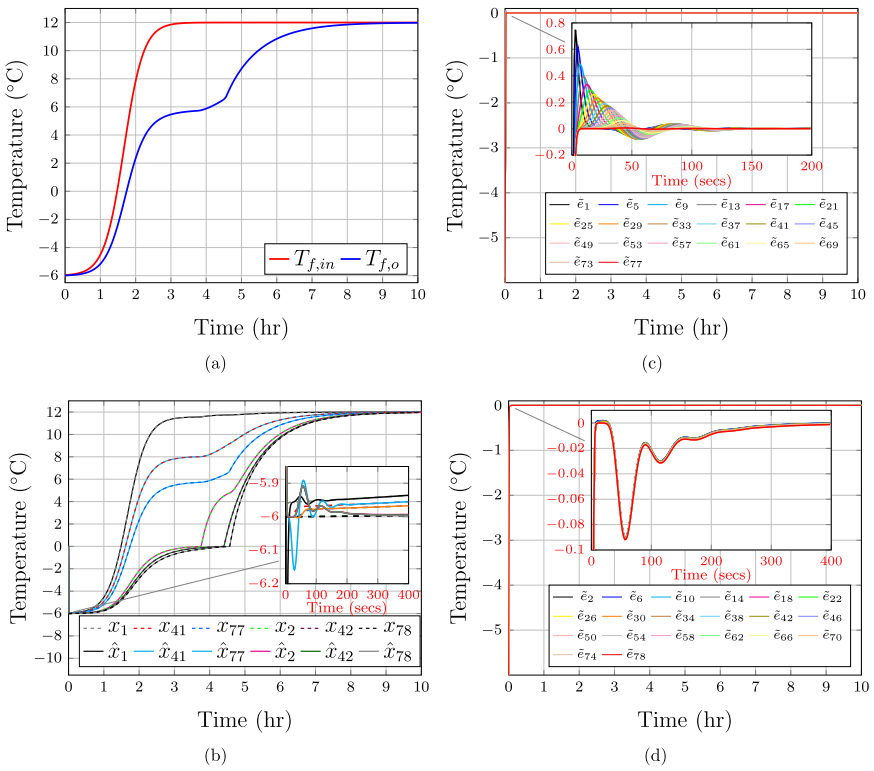

Fig. 11. Performance of the observer for the ice TES tank during the discharging process. (a) Input and output temperatures of the HTF. (b) States of the system and its observer (HTF and PCM temperatures are shown for nodes 1, 11, and 20). Estimation errors for the node temperatures of the (c) HTF and (d) PCM.

modelling approach followed in this paper is based on energy balance. However, some PCM manufacturers directly provide a specific heat–temperature curve, which is obtained by implementing methods such as differential scanning calorimetry or three-layer calorimetry [50,51]. As reported in the literature, this curve may be analytically defined using temperature dependent PDFs [35,40,41].

To further explore this idea, let the specific heat–temperature curve of a fictional PCM with a latent heat value of 5 kJ/kg be described by

$$c_p(T) = 5000\left[\frac{e^{\frac{-(T-\mu)^2}{2\sigma^2}}}{\sigma\sqrt{2\pi}}\right]. \tag{16}$$

Eq. (16) is effectively a Gaussian PDF scaled by the factor 5000 to represent the latent heat value of the PCM, where σ and μ are dimensionless parameters (which, respectively, stand for standard deviation and mean). Scaling is necessary as a Gaussian PDF is a normal distribution which has an integral (area below the curve) equal to 1. The specific enthalpy–temperature curve following integration of (16) is given as

$$h(T) = \int c_p(T)\,dT = 5000\left[\frac{1}{2}\,\mathrm{erf}\left(\frac{T-\mu}{\sqrt{2}\sigma}\right)\right], \tag{17}$$

where 'erf' is the Gauss error function, which is a complex variable function. Within the context of this work, σ and μ are used to define the shape of the specific heat–temperature curve. For instance, a value of $\mu = 20$ would be used to define a melting point at 20 °C, whereas σ would be adjusted to modify the width of the curve.

Fig. 12(a) shows the specific heat–temperature curve of the fictional PCM described by (16), with $\mu = 20$ and $\sigma = 1$. A peak temperature of 20 °C is exhibited. In addition, the specific latent heat is well-defined within the temperature range $T_{\text{empty}} = 16.5$ °C and $T_{\text{full}} = 23.5$ °C. This means that the fictional PCM stores heat when it is liquid. A trapezoidal numerical integration method was adopted to evaluate the specific enthalpy–temperature curve (17) using the MATLAB function *trapz*. Then, it was divided by the specific latent heat, namely $|h|$.

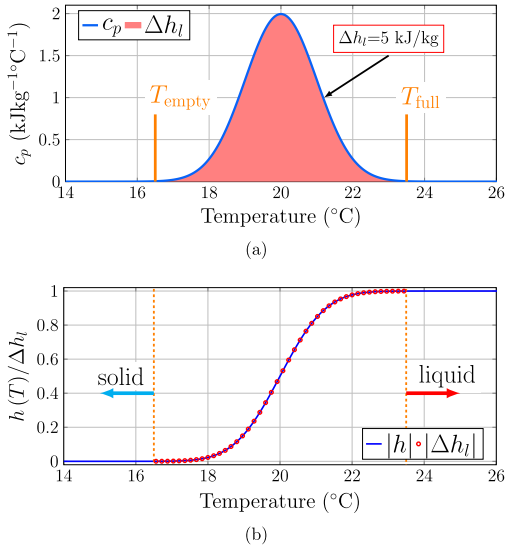

Fig. 12. (a) Specific heat–temperature curve defined by a normal PDF. (b) Integral of the specific heat–temperature curve divided by the specific latent heat.

Fig. 12(b) shows $|h|$, where the minimum value of 0 (dimensionless) at 16.5 °C and the maximum value of 1 (dimensionless) at 23.5° limit the transition zone between solid to liquid, labelled $|\Delta h_l|$.

Eq. (16) enables calculating the amount of specific latent heat by integrating it from T_{empty} to the current PCM temperature T_p [°C]. This value may be employed to determine the SoC of the PCM. If (17) denotes the specific enthalpy–temperature curve for a heating application, the full discharge of the storage unit occurs when solidification has been completely achieved ($T_p \leq T_{\text{empty}}$). Conversely, full charge happens when the PCM is liquid at $T_p \geq T_{\text{full}}$. Thus, for this fictional

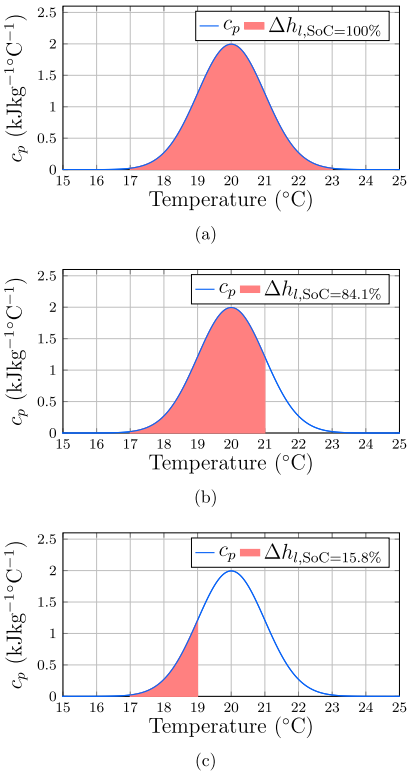

Fig. 13. SoC for three different temperatures. (a) T_p = 24 °C and SoC = 100%. (b) T_p = 21 °C and SoC = 84.1%. (c) T_p = 19 °C and SoC = 15.8%.

example, the SoC is defined within temperatures T_{empty} = 16.5 °C (SoC = 0%) and T_{full} = 23.5 °C (SoC = 100%). This is expressed mathematically as

$$\text{SoC}_T(T) = \begin{cases} 100 & T_p > T_{\text{full}} \\ \dfrac{\int_{T_{\text{empty}}}^{T_p} c_p(T)dT}{\Delta h_l} \times 100 & T_{\text{empty}} \le T_p \le T_{\text{full}} \\ 0 & T_p < T_{\text{empty}} \end{cases}, \tag{18}$$

where the integral of the specific heat–temperature curve evaluated from T_{empty} to T_p is divided by the specific latent heat Δh_l to quantify the percentage of energy (in form of latent heat) remaining in the PCM. The SoC for three different temperatures is shown in Fig. 13 to illustrate this idea. In the figure, the stored latent heat is labelled $\Delta h_{l,\text{SoC}}$ alongside the corresponding value of SoC.

For a cooling application, energy is stored when the PCM solidifies at low temperatures and released when it melts at higher temperatures. T_{full} and T_{empty} thus swap their position in (18) compared to the heating application, yielding

$$\text{SoC}_T(T) = \begin{cases} 0 & T_p > T_{\text{empty}} \\ 100 - \left[\dfrac{\int_{T_{\text{empty}}}^{T_p} c_p(T)dT}{\Delta h_l} \times 100\right] & T_{\text{full}} \le T_p \le T_{\text{empty}} \\ 100 & T_p < T_{\text{full}} \end{cases}. \tag{19}$$

4.2. Implementation of the SoC calculation method

The spatially discretised model presented in Section 2 facilitates this process. If the temperatures of the control volumes in the TES unit models are known, the SoC of the tank is obtained by calculating the average SoC of all N nodes of the tank [35] with

$$\text{SoC} = \frac{\sum_{i=1}^{N} \text{SoC}_{T_i}}{N}, \tag{20}$$

where T_i stands for the temperature at node i.

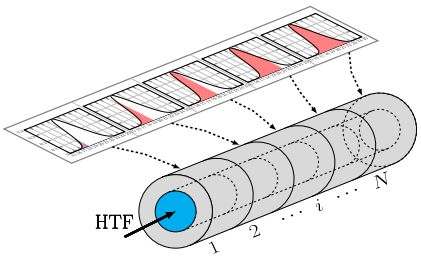

Fig. 14. Illustrative sketch for the SoC calculation method.

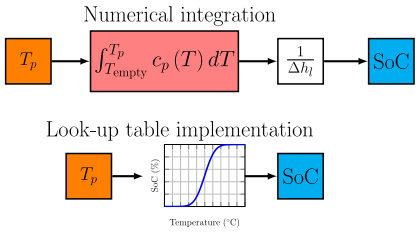

Fig. 15. Schematic of the method for SoC calculation through numerical integration and using a look-up table.

Fig. 16. Block diagram for the implementation of the SoC calculation method using a non-linear observer.

To illustrate the SoC calculation method, a pipe wrapped with a PCM layer is used. This is shown in Fig. 14. During discharging, a 'cold' HTF is circulated inside the pipe to extract the heat stored by the 'hot' PCM. The temperature of the PCM closer to the HTF inlet will decrease faster than the temperature of the PCM near the outlet. Therefore, the latent heat in the PCM control volumes near the inlet will be smaller than for those control volumes close to the outlet, as shown in Fig. 14. Correspondingly, the evaluation of the integral of the specific heat–temperature curve will change as the temperature of the PCM varies during the discharging process.

Based on the previous discussion, the SoC calculation requires evaluating (14) subjected to continuous variations in the temperature of the PCM. By having several control volumes, this calculation may become computationally intensive. To significantly reduce the computational burden, a look-up table was adopted instead, which enables an easier implementation of the method. This approach is illustrated in Fig. 15.

The estimation of the PCM temperatures using the non-linear observer presented in Section 3 enables SoC calculation using the approach presented in Fig. 15. Fig. 16 shows a schematic summarising the complete process for SoC calculation, where temperature and mass flow rate measurements ($T_{f,in}$, $T_{f,o}$ and $\dot{m}_f$) are fed to the observer. The observer outputs, namely the estimated values of PCM temperatures, are used to calculate the SoC using (20).

As shown in the example of Section 4.1, obtaining the SoC curve exclusively requires the specific heat curve of the PCM. This implies that the internal structure of the LHTES unit does not impact SoC calculation. Therefore, a successful implementation of the SoC calculation method depends on the performance of the non-linear observer.

The specific heat curves used to obtain the look-up tables for SoC calculation were adopted from [40,41], where the models of the LHTES units were verified against experimental results for charging and discharging processes. The parameters of these curves are shown in Appendix E. The definition of T_{empty} and T_{full} for the curves is based

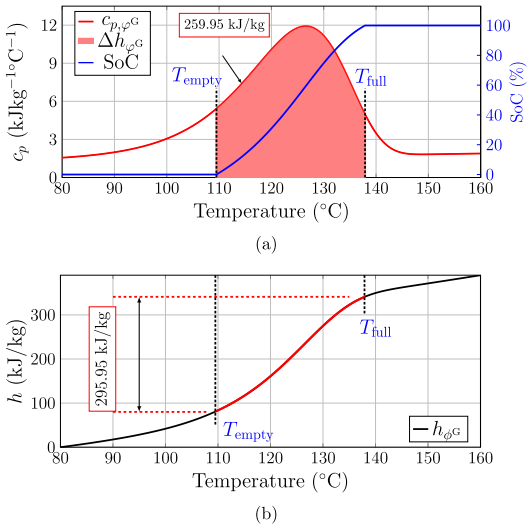

Fig. 17. (a) Specific heat–temperature curve of the PCM for the shell and tube TES unit and SoC calculation using the look-up table. (b) Specific enthalpy calculation using (14).

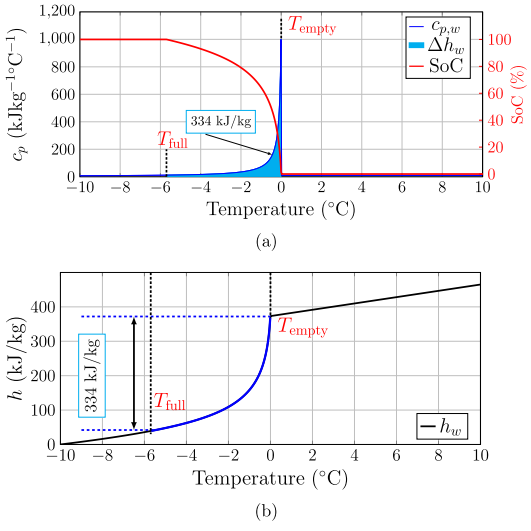

Fig. 18. (a) Specific heat–temperature curve of the PCM (water) for the ice TES tank as in [40] and SoC calculation using the look-up table. (b) Specific enthalpy calculation using (14).

on the latent heat value reported in [40] for water and in [41] for Rigidex HD6070EA. Other specific considerations of SoC calculation for the shell and tube TES unit and for the ice TES tank are discussed in the following subsections.

4.2.1. SoC calculation for the shell and tube TES unit

This was done using the PDF included in Appendix E (Gumbel minimum distribution) and illustrated in Fig. 17. Fig. 17(a) shows the specific heat–temperature curve of the PCM (Rigidex HD6070EA, see the red trace labelled c_{p,φ^G}). The look-up table for SoC calculation was obtained using the specific heat–temperature curve, Eq. (18), and the specific latent heat $\Delta h_{\varphi^G} = 259.95$ kJ/kg. Δh_{φ^G} was obtained using (15) and represented by the area below the specific heat–temperature curve using a red shading. The transition zone where the latent heat is absorbed or released and the trace of the SoC (see blue trace) fully match. This implies that once the PCM has a temperature $T_{\text{empty}} = 109.5$ °C, the TES unit is considered as fully discharged (SoC = 0%). A full charge is reached when the PCM temperature is above $T_{\text{full}} = 138$ °C (SoC = 100%). Fig. 17(b) shows the specific enthalpy–temperature curve (denoted h_{φ^G}) obtained using (14), where T_{empty} and T_{full} are clearly identified to highlight the specific latent heat.

4.2.2. SoC calculation for the ice TES tank

A PDF included in Appendix E (Lognormal distribution) is used to define the specific heat–temperature curve for water in [40] and reproduced in Fig. 18(a). The specific latent heat ($\Delta h_w = 334$ kJ/kg) is represented by the area below the specific heat–temperature curve (see blue trace labelled $c_{p,w}$) using a light blue shading. This area is limited by $T_{\text{full}} = -5.7$ °C and $T_{\text{empty}} = 0$ °C. The figure includes the SoC calculation using (19), whose value is 100% when the water reaches temperature T_{full} (i.e. full charge). A complete discharge occurs when the water has a temperature above T_{empty}. For this cooling application, the SoC curve and the location of T_{full} and T_{empty} are inverted when compared with the heating application. The specific enthalpy–temperature curve (denoted h_w) is shown in Fig. 18(b), where the specific latent heat Δh_w is also highlighted and limited by T_{full} and T_{empty}.

5. Quantification of sensible and latent heat

Both sensible and latent heat contribute simultaneously to the charging and discharging processes of LHTES units. Distinguishing the contribution from each heat source in a real system is a challenging task, although a good mathematical model of the thermal store may enable this. Sensible heat was not considered in (18) and (19) to prevent overcomplicating the SoC calculation. However, clearly identifying its contribution will help assessing the validity of the presented method.

The contribution of sensible heat depends on the initial and the operating conditions of the storage units. For instance, if the initial temperature of the PCM is far from T_{empty} or T_{full}, the available sensible heat is considerably large. Conversely, if the initial temperature is close to T_{empty} or T_{full}, it is significantly low.

The quantification of the heat provided by the latent and sensible heat was obtained using the node temperatures of the PCM and Eq. (2) while restricting it with T_{empty} and T_{full}. Thus, the latent heat contribution q_l [J/s] to the heat transfer process for heating applications is given by

$$q_l = \begin{cases} 0 & T_p > T_{\text{full}} \\ U A_{tr} \left(T_f - T_p\right) & T_{\text{empty}} \le T_p \le T_{\text{full}} \\ 0 & T_p < T_{\text{empty}} \end{cases}, \tag{21a}$$

whereas for cooling applications it is described by

$$q_l = \begin{cases} 0 & T_p > T_{\text{empty}} \\ U A_{tr} \left(T_f - T_p\right) & T_{\text{full}} \le T_p \le T_{\text{empty}} \\ 0 & T_p < T_{\text{full}} \end{cases}. \tag{21b}$$

The sensible heat q_s [J/s] contribution for a heating application is calculated with

$$q_s = \begin{cases} U A_{tr} \left(T_f - T_p\right) & T_p > T_{\text{full}} \\ 0 & T_{\text{empty}} \le T_p \le T_{\text{full}} \\ U A_{tr} \left(T_f - T_p\right) & T_p < T_{\text{empty}} \end{cases}, \tag{22a}$$

whereas for a cooling application it is defined by

$$q_s = \begin{cases} U A_{tr} \left(T_f - T_p\right) & T_p > T_{\text{empty}} \\ 0 & T_{\text{full}} \le T_p \le T_{\text{empty}} \\ U A_{tr} \left(T_f - T_p\right) & T_p < T_{\text{full}} \end{cases}. \tag{22b}$$

These amounts were compared with the total HTF power P_T during charging and discharging, which is defined by

$$P_T = \dot{m}_f c_{p,f} \left(T_{f,in} - T_{f,o}\right). \tag{23}$$

The specific contribution from each heat source is graphically identified for both LHTES units in the following subsections.

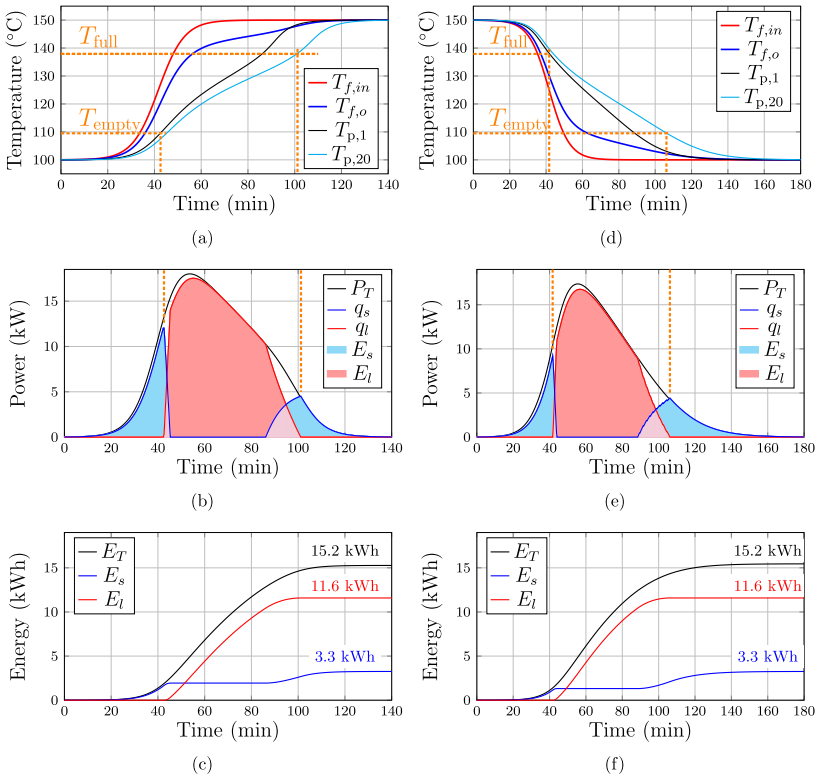

Fig. 19. Simulation results for the shell and tube TES unit. Charging process: (a) input and output temperatures of the HTF and temperature of PCM nodes 1 and 20; (b) thermal power given by the HTF and contributions from latent heat and sensible heat; (c) total energy and energy provided by latent heat and sensible heat. Discharging process: (d) input and output temperatures of the HTF and temperature of PCM nodes 1 and 20; (e) thermal power given by the HTF and contributions from latent heat and sensible heat; (f) total energy and energy provided by latent heat and sensible heat.

5.1. Shell and tube TES unit

The mathematical model presented in [42] was used to simulate charging and discharging processes, with results shown in Fig. 19. For charging, the HTF input temperature was increased to a maximum value $T_{f,in} = 150$ °C, while all initial HTF and PCM node temperatures were set to 100 °C. Conversely, for discharging the HTF input temperature was decreased to a minimum value $T_{f,in} = 100$ °C with all initial conditions of temperature set at 150 °C. For both simulations, a constant mass flow rate of 1.03 kg/s was used. Figs. 19(a) and 19(d) show the input and output temperatures of the HTF ($T_{f,in}$ with a red trace and $T_{f,o}$ with a blue trace) for charging and discharging, respectively. Only the PCM temperatures of nodes 1 and 20 are presented for clarity.

Figs. 19(b) and 19(e) show the charging and discharging power P_T (see black traces) obtained with (23). The total energy provided by the latent heat is given by the area below the power curve q_l (red traces). Similarly, the total energy provided by the sensible heat is given by the area below q_s (blue traces). The shaded red area E_l [J] explicitly highlights the latent heat and the shaded blue area E_s [J] the sensible heat. For the discharging process, to prevent showing negative values of power as $T_{f,in}$ is lower than the initial conditions of the node temperatures, the results were multiplied by −1.

Dashed orange lines were added in Figs. 19(a), 19(b), 19(d) and 19(e) to highlight when node 1 reaches temperature $T_{empty} = 109.5$ °C and when node 20 reaches $T_{full} = 138$ °C. This was done to show when the contribution of latent heat starts and finishes. The absorption of latent heat thus initiates when the temperature of the first node of the PCM ($T_{p,1}$) reaches T_{empty} and the provision of sensible heat declines. The absorption of latent heat finishes when the last node of the PCM ($T_{p,20}$) reaches T_{full}.

As shown in Fig. 19(b), sensible heat also contributes to charging once the temperature of the PCM in the first node reaches T_{full} (when full charging has been almost achieved). This means that the increment of the temperature for all other nodes reaching T_{full} will be achieved by the absorption of sensible heat only.

Figs. 19(c) and 19(f) show the total energy provided by the HTF for charging and discharging, respectively, in terms of the heat source. Latent heat contributes 11.6 kWh (76.3%) and sensible heat 3.3 kWh (21.7%) of the total energy (15.2 kWh) for either process. These values were obtained by calculating the integral of the corresponding power curves shown in Figs. 19(b) and 19(e).

5.2. Ice TES tank

A simulation with a 20-nodes discretised model was conducted to quantify the energy stored during charging and discharging processes of the ice TES tank, with results shown in Fig. 20. A HTF input temperature varied between −6°C to 12 °C was used. Constant mass flow rates of 20 kg/s and 5 kg/s were used for charging and discharging processes, respectively. Figs. 20(a) and 20(d) show the temperature of the HTF entering and leaving the tank ($T_{f,in}$ with a red trace and $T_{f,o}$ with a blue trace) and the PCM temperatures (i.e. water) in nodes 1 and 20 of the mathematical model. In this case, the power during charging was multiplied by −1 to prevent showing negative values.

T_{empty} and T_{full} have been highlighted in Figs. 20(a), 20(b), 20(d) and 20(e) to show the beginning and the end of the release or absorption of latent heat. The contribution of sensible heat is shown at the beginning of the charging process (see Fig. 20(b)). This starts to decrease when the temperature of the PCM in the first node ($T_{w,1}$) reaches T_{empty}, and finishes when the temperature in the last node ($T_{w,20}$) also reaches this value. Conversely, the latent heat contribution starts when $T_{w,1} = T_{empty}$ and finishes when $T_{w,20} = T_{full}$. Once the PCM is completely charged, only sensible heat is present. For discharging, the sensible heat contribution lasts until $T_{w,20} = T_{full}$ (see Fig. 20(e)). The latent heat contribution starts when $T_{w,1} = T_{full}$ and lasts until $T_{w,20} = T_{empty}$.

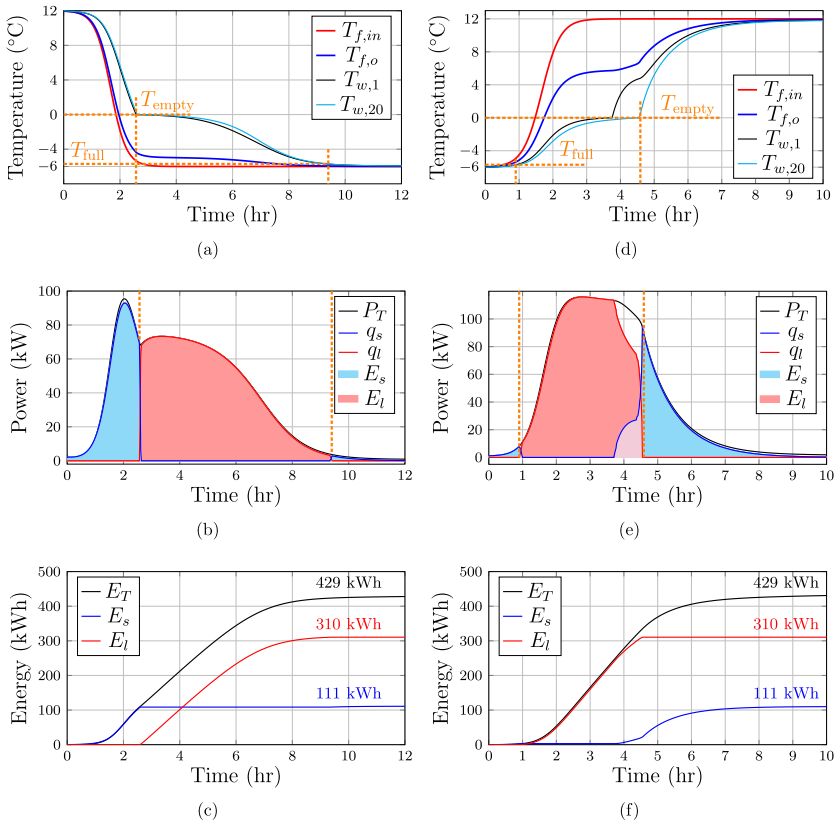

Fig. 20. Simulation results for the ice TES tank. Charging process: (a) input and output temperatures of the HTF and temperature of PCM nodes 1 and 20; (b) thermal power given by the HTF and contributions from latent heat and sensible heat; (c) total energy and energy provided by latent heat and sensible heat. Discharging process: (d) input and output temperatures of the HTF and temperature of PCM nodes 1 and 20; (e) thermal power given by the HTF and contributions from latent heat and sensible heat; (f) total energy and energy provided by latent heat and sensible heat.

The energy provided by each heat source is shown in Fig. 20(c) for charging and Fig. 20(f) for discharging, which were obtained by calculating the integral of the power curves (given in Fig. 20(b) and Fig. 20(e), respectively). A similar contribution of sensible heat is shown in both processes since the same operating range for $T_{f,in}$ was used and the same initial conditions for HTF and PCM nodes were adopted. The latent heat accounts for 72% of the total energy absorbed or released.

Note: As the phase change in a PCM occurs irregularly throughout the volume of an LHTES unit, accurately quantifying the sensible heat contribution to the SoC is a challenging task. In addition, the contribution of sensible heat to the energy stored or supplied by the unit will depend on the charging and discharging processes defined by the input temperature of the HTF. To prevent the SoC calculation method from becoming too complex, the transition zone where the phase change of the PCM occurs is considered only, which is well-defined by the PCM's specific heat curve. This approach also exploits the main attribute of a PCM, which is its large storage capacity during phase change. Such an idea is supported by commercial manufacturers, which define the storage capacity of a TES unit as the total mass of the PCM times its latent heat value [52–54]. The temperature range of the phase change is critical for selecting an LHTES unit for a specific application as this determines the ideal charging and discharging temperatures to support a thermal process.

6. Results

To assess the performance of the SoC calculation method presented in this paper, simulations of the mathematical models of the LHTES units discussed in Section 2 were conducted and compared against experimental data available in the literature. Validity of these models was verified in [40,42]. Fig. 21(a) shows the schematic illustrating the approach here followed. Screenshots depicting the implementation in MATLAB/Simulink of the model of the TES unit, the non-linear observer, the definition of the SoC look-up table, and the charging/discharging power calculation are shown in Fig. 21(b). MATLAB/Simulink S-functions were used to code both the dynamic model of the thermal store and its non-linear observer

To assess the performance of the non-linear observer and the SoC calculation method, the next steps were followed for a sequence of charging and discharging processes: (1) definition of the look-up table for SoC calculation based on the specific heat–temperature curve of the PCM (using (18) for the heating application or (19) for the cooling application), (2) quantification of the sensible and latent heat for charging an discharging using (21) and (22), and (3) SoC calculation using observer outputs (estimated PCM temperatures) and employing (20).

6.1. Shell and tube TES unit

To verify the performance of the 1-D dynamic model, its observer and the SoC calculation method, simulation results during a sequence of charging and discharging processes were compared with experimental data presented in [41]. The experimental data is constituted by three key measurements: the output temperature of the HTF, the total supplied energy by the TES unit and its SoC. A discretised mathematical model of the TES unit with 20 nodes was employed in the simulation. Similarly, the non-linear observer was discretised into 20 nodes. A constant mass flow rate of 1.09 kg/s was used. The initial temperature conditions for the model of the TES unit and the observer states were set to 80 °C and 50 °C, respectively. A Gumbel minimum distribution was used to define the specific heat–temperature curve (see Section 4.2

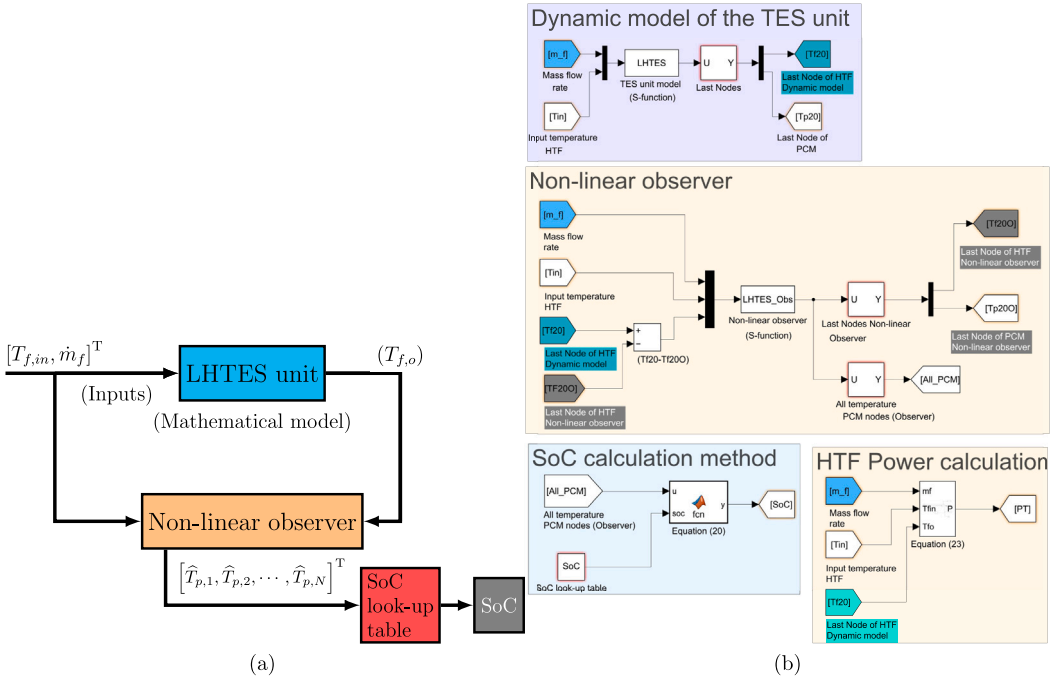

Fig. 21. (a) Block diagram of the LHTES unit model, non-linear observer and SoC look-up table. (b) Screenshot of the implementation in MATLAB/Simulink: S-function of the 1-D model of the TES unit, S-function of the non-linear observer, and SoC look-up table and calculation of the HTF power.

and Appendix E). The plots of the simulated and the experimental results are shown together for a graphical comparison. To provide a numerical quantification of the agreement between simulation results with the experimental data, an error analysis was conducted. This analysis consists of calculating the root mean square error (RMSE) and the mean absolute error (MAE) for each variable with respect to the experimental data.

Fig. 22(a) shows the HTF input and output temperature profiles $T_{f,in,exp}$ (red trace) and $T_{f,o,exp}$ (blue trace) used in the experiments, where subscript 'exp' is used to denote experimental data. The HTF input temperature profile was fed to the mathematical model. The output temperature of the HTF obtained through simulation is shown (solid black trace, defined by the temperature of the last node, $T_{f,20} = T_{f,o,sim}$, where subscript 'sim' denotes simulation results). The estimated temperature of the last node of the model is an output of the observer (dashed grey trace, $\widehat{T}_{f,20} = T_{f,o,obs}$), also shown in the graph. An error analysis of the simulated output temperature of the HTF ($T_{f,o,sim}$) with respect to the experimental data ($T_{f,o,exp}$) demonstrates the accuracy of the 1-D model, with an RMSE of 2.13 °C and an MAE of 1.81 °C, which represent 1.33% and 1.13%, respectively, of the maximum value this variable may take (i.e. 160 °C, which is the maximum input temperature of the HTF). Moreover, the observer can estimate the HTF output temperature ($T_{f,o,sim}$) with an estimation error ($T_{f,o,sim} - T_{f,o,obs}$) quickly converging to zero during the simulation period (see Fig. 23).

The estimated states for nodes 1, 11 and 20 ($\hat{x}_1$, $\hat{x}_{21}$ and $\hat{x}_{39}$ for the HTF, $\hat{x}_2$, $\hat{x}_{22}$ and $\hat{x}_{40}$ for the PCM) are shown in Fig. 22(b) and presented alongside the states from the mathematical model of the TES unit (x_1, x_{21} and x_{39} for the HTF, and x_2, x_{22} and x_{40} for the PCM). As it can be seen, the states of the model are accurately estimated by the observer during the simulation.

Fig. 23 shows the estimation error for all 40 states, with Fig. 23(a) illustrating the HTF temperatures and Fig. 23(b) the PCM temperatures. The observer had a successful performance for the whole simulation period, reducing all estimation errors to zero in less than 300 s even when there is a difference of 30 °C between the initial conditions of the TES unit model and observer. The match of the experimental profile $T_{f,o,exp}$ (blue trace) with the estimated output temperature of the HTF $T_{f,o,obs}$ (dashed grey trace) is further assessed by calculation of the RMSE and

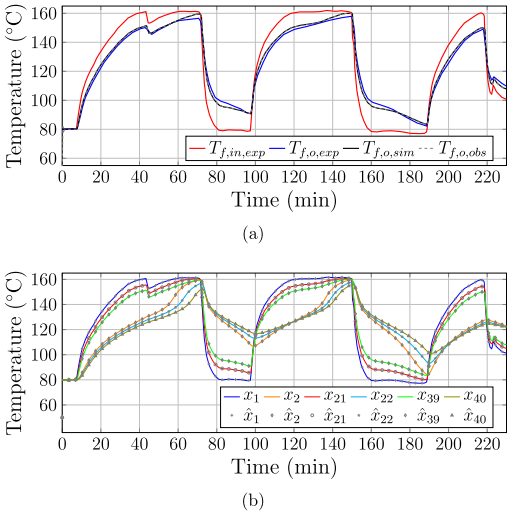

Fig. 22. (a) Experimental input temperature of the HTF, and experimental, simulated, and estimated output temperature of the HTF for the shell and tube TES unit. (b) Comparison of the actual state and estimated state variables of the mathematical model and the non-linear observer for nodes 1, 11 and 20.

MAE, yielding 2.21 °C and 1.84 °C, which respectively represent 1.38% and 1.15% of the maximum value for HTF temperature. These values are very close to those obtained from the simulation model, providing confidence in both the performance of the 1-D model adopted in this paper and the non-linear observer design.

The total stored energy (E_T) and the SoC calculated during the simulation were compared with those reported in [41], with results shown in Fig. 24. Experimental ($E_{T,exp}$) and simulated total energies ($E_{T,sim}$) are shown in Fig. 24(a). In this case, the RMSE is 0.57 kWh and the MAE is 0.49 kWh, which represent, respectively, 3% and 1.6% of the maximum value (18.5 kWh). These small errors confirm the high accuracy of the mathematical model. The contributions of latent heat and sensible heat, $E_{l,sim}$ and $E_{s,sim}$, to $E_{T,sim}$ are presented in Fig. 24(b).

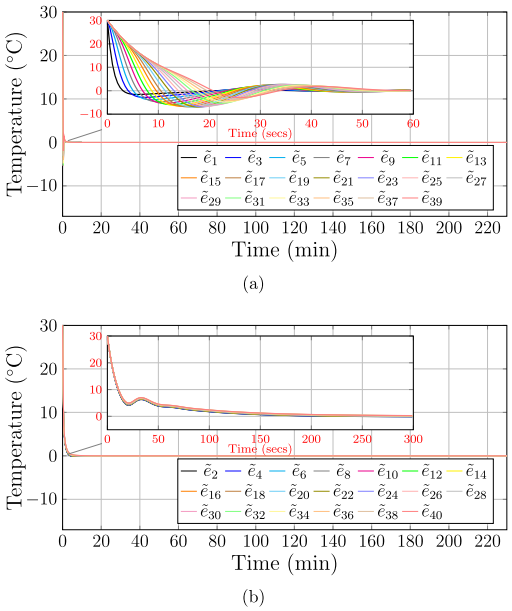

Fig. 23. Estimation errors for the shell and tube TES unit during a sequence of charging and discharging processes. Temperatures of the (a) HTF and (b) PCM.

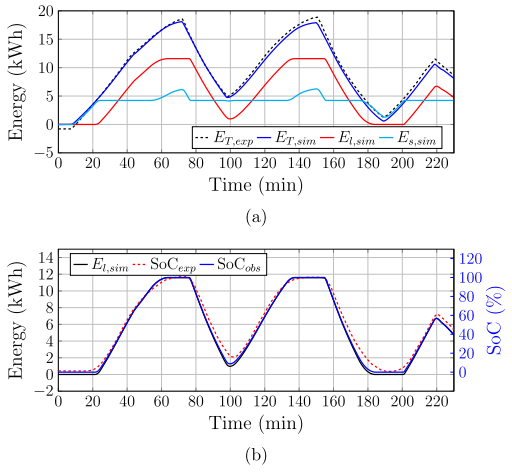

Fig. 24. (a) Experimental and simulated total stored energy by the shell and tube TES unit, and energy provided by latent heat and sensible heat. (b) Comparison between the SoC and the energy provided by the latent heat reported by [41] with the SoC given by the proposed method.

The experimental data for SoC reported in [41] (see dashed red trace SoC_{exp}) and the SoC calculated with the method presented in this paper (blue trace SoC_{obs}) are very close through the whole simulation, exhibiting an RMSE of 4.58% and an MAE of 3.61%. The contribution of the energy provided by the latent heat (solid black trace $E_{l,sim}$) is also shown in Fig. 24(b) to afford a graphical comparison. The match between the graphs and the small errors give confidence in the validity of the presented method for SoC calculation, which only considers the contribution of latent heat — facilitated by the successful performance of the non-linear observer as previously described.

For completeness, Table 1 summarises the information on the error analysis.

6.2. Ice TES tank

The non-linear observer and the SoC calculation method were assessed for two complete charging and discharging cycles of the ice TES tank under variations in the mass flow rate of the HTF. Simulation results are shown in Fig. 25. Since a large mass flow rate is required to conduct charging within a reasonable period for practical applications, values of 22 kg/s and 19 kg/s were employed (see Fig. 25(a)). Fig. 25(b) shows how the error between the output temperature of the HTF (see the solid black trace $T_{f,o}$) and the estimated value (dashed grey trace, $T_{f,o,obs}$) is reduced to zero early in the first discharging process. A reduced mass flow rate for the second charging cycle (conducted at 19 kg/s), starting from around 24 h into the simulation, slightly increases the time for achieving full charge. For clarity, the temperatures of nodes 1, 11 and 20 for tube 'a' only (x_1, x_{41} and x_{77} for the HTF, x_2, x_{42} and x_{78} for the PCM) are compared with their corresponding estimated states ($\hat{x}_1$, $\hat{x}_{41}$ and $\hat{x}_{77}$ for the HTF, and $\hat{x}_2$, $\hat{x}_{42}$ and $\hat{x}_{78}$ for the PCM) in Fig. 25(c). The observer accurately estimates the temperature of the HTF and PCM nodes throughout even when there is a sharp change in the input temperature of the HTF while discharging at around 17 h and 34 h into the simulation (see Fig. 25(c)).

Fig. 26 shows the observer estimation errors. The observer performance is adequate, with the errors converging to zero within the first 200 s of the simulation. However, the errors of the PCM temperatures slightly increase at around 4.5 h (see the zoomed-in enclosed plot within Fig. 26(b)). These increments occur when the phase change of the PCM has been completed and only sensible heat is present. This produces a sudden change in temperature, as seen in the profiles of states x_2, x_{42} and x_{78} in Fig. 25(c). However, the observer reduces all errors to zero after approximately 1.5 h. The maximum value of these errors before convergence to zero is about 0.1 °C, without causing significant impact in SoC calculation.

Table 1
RMSE and MAE of simulated and observed output temperature of HTF ($T_{f,o,sim}$, $T_{f,o,obs}$), SoC and total energy (E_T) with respect to experimental data.

	$T_{f,o,sim}$ [°C]	$T_{f,o,obs}$ [°C]	SoC [%]	E_T [kWh]
RMSE	2.13	2.21	4.58	0.57
MAE	1.81	1.84	3.61	0.49

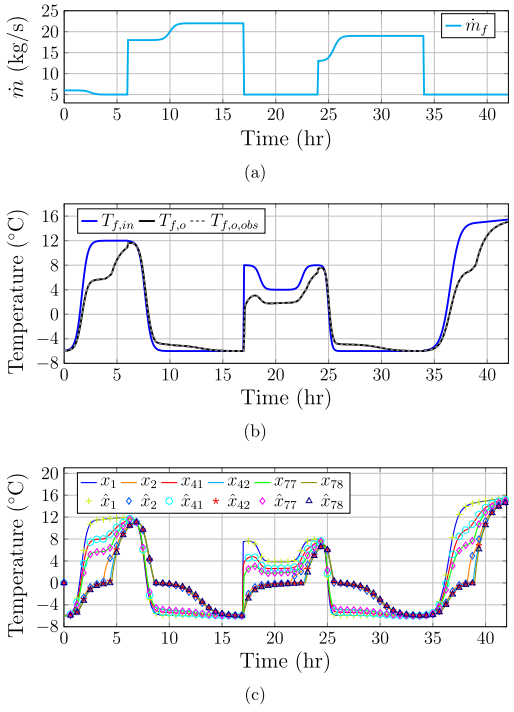

Fig. 25. Results for the ice tank. (a) Mass flow rate profile. (b) Input and output temperature of the HTF given by the mathematical model, and estimated output temperature of the HTF. (c) Comparison between the actual state variables and the estimated state variables for nodes 1, 11 and 20.

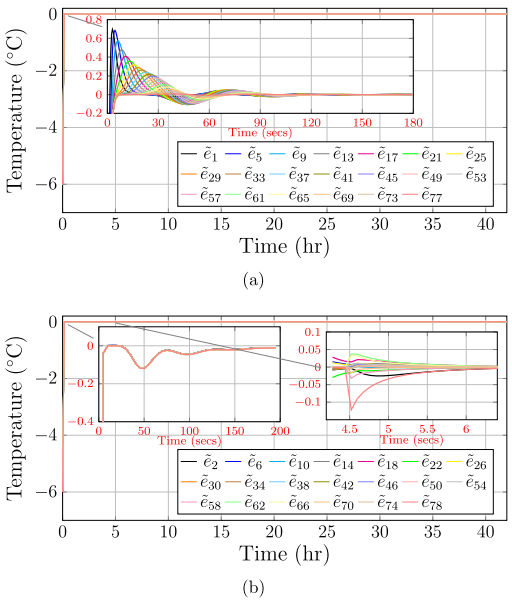

Fig. 26. Estimation errors for the ice TES tank during a sequence of charging and discharging processes. Temperatures of the (a) HTF and (b) PCM.

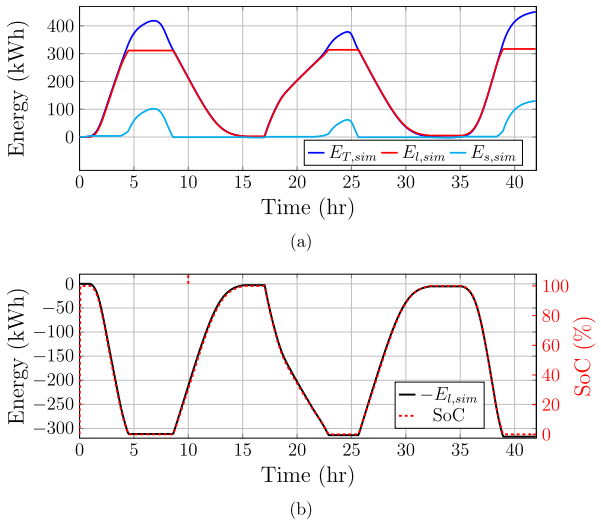

Fig. 27. (a) Total stored energy by the ice TES tank and energy provided by latent heat and sensible heat. (b) Comparison between the SoC calculated by the proposed method and the energy provided by the latent heat.

The total energy ($E_{T,sim}$) and the contribution of latent heat ($E_{l,sim}$) and sensible heat ($E_{s,sim}$) are shown in Fig. 27(a). At the end of each discharging process the total latent heat supplied as cooling is 310 kWh. This means that the stored energy increases to release the cooling. Conversely, the stored energy decreases during each charging process as the PCM temperature is decreased to harvest ice. Therefore, to compare with the SoC curve, the energy provided by latent heat is multiplied by −1. Fig. 27(b) shows the latent heat profile ($E_{l,sim}$) and the SoC. The initial value of SoC is 0% because the initial conditions of the observer were set to 0 °C. Nevertheless, after the estimation error is reduced to zero the SoC agrees well with the latent heat profile. This verifies the accuracy of the presented method for SoC calculation using the estimated values of the PCM temperature inside the ice TES tank.

7. On the limitations of the presented work

The simulation results presented in the paper have demonstrated that simplified dynamic 1-D models of LHTES units are sufficient to estimate the internal temperatures of the storage medium. Nevertheless, this process heavily depends on the availability of the thermophysical properties of the elements involved in the heat transfer: the HTF, the PCM and the material of the tubes enclosing the HTF. Although some PCM and TES manufacturers provide this information, in some cases it may not be publicly available. In addition, both the 1-D dynamic model and its non-linear observer require the parameters and dimensions of the internal geometry of the thermal store. This information may not be disclosed by manufacturers.

Although the non-linear observers and the SoC calculation methods achieve a successful performance when adopting the 1-D models borrowed from [40,42], these in the end are simplified representations of complex dynamic systems. For instance, some dynamic phenomena, such as supercooling, are not reproduced by the models. Supercooling occurs when a liquid does not solidify even if its temperature is lower than the crystallisation point [55], and this can be attributed to the primary nucleation of a PCM and the mechanism of crystal growth. However, the effects of supercooling are challenging to incorporate to 1-D or 2-D models. Investigating supercooling and its effect on SoC estimation is a topic that requires further investigation.

It should be noted that the presented method for SoC estimation was verified under specific operating conditions for charging and discharging. Conducting additional experiments which consider variations in the input temperature and mass flow rate of the HTF may help to increase reliability of the method for a wide operating range. In addition, verifying the SoC estimation method for thermal stores with a different internal geometry from the ones investigated in the paper would be desirable to extend the range of applications that could benefit from it.

8. Conclusions

The effective control over the charging and discharging processes of LHTES units is necessary to improve the performance of thermal systems where they are employed. To develop adequate control strategies that maximise the use of these thermal stores, SoC monitoring is critical. Following this line, a non-linear observer to estimate the temperatures of the HTF and PCM inside an LHTES unit and a SoC calculation method were presented and assessed in this paper. The accurate estimation of the internal states of the storage unit afforded by the state observer enables SoC calculation with no need to install internal temperature sensors. As it has been demonstrated, only the measurements of the mass flow rate and the input and output temperatures of the HTF are necessary for an accurate estimation. Thus, a costly direct measurement for SoC calculation is relieved by the proposed approach.

Two different LHTES units were analysed in this work. A shell and tube TES unit was investigated for a heating application and an ice TES tank was assessed for a cooling application. The performance of their respective observer was evaluated by comparing simulation results with experimental data available from references. The observer design was based on highly accurate and validated 1-D dynamic models (also available in the literature). These models are substantially simpler than representations requiring computational fluid dynamics. To initialise the observers, although there are no established criteria to define their initial conditions, setting up these values near the melting temperature of the PCM would speed up the initial estimation of the system states. Charging and discharging operation modes were assessed. Simulation results show a good performance of the observers for both applications, ensuring convergence of the estimation errors of the HTF and PCM temperatures to zero within 5 min.

The SoC was defined as the mean of the latent heat released (or absorbed) by the PCM inside the storage units. A look-up table for SoC calculation was implemented based on the specific heat–temperature curve and the PCM temperature. Such an approach reduces the computational burden from methods based on numerical integration. The presented SoC calculation method performs well using the observer's estimated temperatures. This is evidenced by the small errors in the SoC calculation when compared to the available experimental data, with values of less than 4.6% in RMSE and 3.62% in MAE.

The results in this paper demonstrate that an effective SoC calculation depends only on the availability of an accurate 1-D dynamic model of the TES unit and knowledge of the thermophysical properties of the PCM, which are usually provided by manufacturers. This was demonstrated using two LHTES units with different internal geometries and intended for different applications (one for heating and one for cooling). Thus, the SoC calculation approach based on a suitably designed observer represents a feasible and reliable option for the management of LHTES units.

CRediT authorship contribution statement

Hector Bastida: Conceptualization, Methodology, Software, Validation, Formal analysis, Investigation, Writing – original draft, Visualization. **Ivan De la Cruz-Loredo:** Conceptualization, Methodology, Software, Formal analysis, Writing – review & editing. **Carlos E. Ugalde-Loo:** Conceptualization, Formal analysis, Resources, Writing – original draft, Software, Visualization, Project administration, Funding acquisition.

Declaration of competing interest

The authors declare that they have no known competing financial interests or personal relationships that could have appeared to influence the work reported in this paper.

Data availability

Data will be made available on request.

Acknowledgements

The work presented in this paper was funded by the National Council for Science and Technology of Mexico (CONACyT). The work was also supported by FLEXIS. FLEXIS is part-funded by the European Regional Development Fund (ERDF), through the Welsh Government (WEFO case number 80836). This work was also supported by the Engineering and Physical Sciences Research Council (EPSRC), UK Research and Innovation (UKRI), through the project 'Flexibility from Cooling and Storage (Flex-Cool-Store)', Grant EP/V042505/1.

Appendix A. Derivation of equations for energy balance

From the energy conservation law for a control volume, the rate of change in the energy stored $\dot{E}_{st}$ [J/s] is defined by

$$\dot{E}_{st} = \dot{E}_{in} - \dot{E}_{out}, \tag{A.1}$$

where $\dot{E}_{in}$ [J/s] stands for the energy inflows and $\dot{E}_{out}$ [J/s] for the energy outflows. Let $\dot{E}_f$ [J/s] be the rate of change of the energy stored by an HTF and q represent a heat rate. Eq. (A.1) is rewritten as

$$\dot{E}_f = q_{in} + q_{tr}. \tag{A.2}$$

With reference to Fig. 3, q_{in} [J/s] in (A.2) is the heat rate provided by an external source, in this case the input of the HTF crossing the tube, and q_{tr} [J/s] is the heat rate resulting from the energy transferred to or from the PCM through the tube's wall. For a 1-D modelling approach, (A.2) describes how the mean temperature of the HTF varies with respect to the x direction along a horizontal tube. To reduce modelling complexity, viscous dissipation, radial fluid flow, axial heat conduction, external forces, and compressibility are neglected as in [40,41]. This way, the heat transferred to a control volume of the HTF is defined in terms of the rate of change of its internal energy E_f [J] as

$$\dot{E}_f = m_f c_{p,f} \dot{T}_f, \tag{A.3}$$

where m_f [kg] is the mass of the HTF, $c_{p,f}$ [J/(kg°C)] its specific heat (dependent of the HTF temperature), and $\dot{T}_f$ is the rate of change in the mean temperature of the HTF's mass. The difference between the input and the mean temperatures of the HTF in the control volume defined in Fig. 3 causes a forced convection heat rate (q_{in}). This is mathematically expressed as

$$q_{in} = \dot{m}_f c_{p,f} \left(T_{f,in} - T_f\right). \tag{A.4}$$

The heat transferred between the HTF and the PCM, q_{tr}, depends on their temperature difference as well, and it is calculated using the overall heat transfer coefficient U [W/(m²°C)] as [56]

$$q_{tr} = U A_{tr} \left(T_p - T_f\right), \tag{A.5}$$

where A_{tr} [m²] is the heat transfer area and T_p [°C] is the mean temperature of the volume of the PCM. Substituting (A.3), (A.4) and (A.5) into (A.2), the energy balance of the control volume of the HTF is expressed as

$$m_f c_{p,f} \dot{T}_f = \dot{m}_f c_{p,f} \left(T_{f,in} - T_f\right) + U A_{tr} \left(T_p - T_f\right). \tag{A.6}$$

The initial and boundary conditions of (A.6) are given by

$$T_f\left(t = 0, x\right) = T_f^0\left(x\right), \quad T_f\left(t, x = 0\right) = T_{f,in}\left(t\right). \tag{A.7}$$

Notice that (1) is obtained simply by substituting (A.4) and (A.5) into (A.2).

Following the same approach, the rate of change of the internal energy of the PCM, $\dot{E}_p$ [J/s], is derived. Since there is no external heat source in this case, $\dot{E}_p$ is only affected by the heat transferred by the HTF, namely,

$$\dot{E}_p = m_p c_{p,p} \dot{T}_p = U A_{tr} \left(T_f - T_p\right), \tag{A.8}$$

where m_p [kg] is the mass of the control volume of the PCM and $c_{p,p}$ [J/(kg°C)] its specific heat (which is dependent of the PCM temperature).

Notice that (A.8) is the same as (2). The initial and boundary conditions of (A.8) are given by

$$T_p\left(t = 0, x\right) = T_p^0\left(x\right), \quad T_p\left(t, x = 0\right) = T_f\left(t\right). \tag{A.9}$$

Appendix B. Properties and parameters of the LHTES units

Relevant information of the shell and tube TES unit is provided in Table B.2.

Table B.2
Parameters of shell and tube TES unit (single tube) [41,42].

Parameter	Symbol	Value	Unit
Tube external radius	r_o	8.25	mm
Tube internal radius	r_i	6.75	mm
Tube hydraulic diameter	D_t	13.5	mm
Tube length	L	2.5	m
Heat transfer area	A_{tr}	0.1060	m²
Cross sectional area	A_c	1.4314×10^{-4}	m²
HTF volume	V_f	3.5785×10^{-4}	m³
Thermal conductivity of the tube (carbon alloy steel P235GH)	k_t	50	W/(m°C)
Radius of PCM	r_p	19.9774	mm
Cross sectional area of PCM	A_p	0.00104	m²
PCM volume	V_p	0.0026	m³

Table B.3
Parameters of ice TES tank (single tube) [40].

Parameter	Symbol	Value	Unit
Tube external radius	r_o	7.9375	mm
Tube internal radius	r_i	6.35	mm
Tube hydraulic diameter	D_t	12.7	mm
Tube length	L	32.5581	m
Heat transfer area	A_{tr}	1.6238	m^2
Cross sectional area	A_c	1.266×10^{-4}	m^2
HTF volume	V_f	0.0041	m^3
Thermal conductivity of the tube (polyethylene)	k_t	0.33	W/(m°C)
Water/ice thermal conductivity	k_w	1.35	W/(m°C)
Ice radius	r_w	23.9395	mm
Cross sectional area of ice	A_w	0.0016	m^2
Surface area	A_{ex}	4.9	m^2
Ice volume	V_w	0.0522	m^3

Note: An average value of the thermal conductivity of liquid water/ice is assumed during the phase transition, as the model in [40] does not calculate the liquid or solid fraction of water during phase change and only considers the energy released during this transition.

The thermophysical properties of the HTF (Marlotherm SH) are given by the following temperature dependent equations:

$$\rho_f = -0.71482T + 1058.4, \tag{B.1}$$

$$c_{p,f} = 3.7263T + 1474.5, \tag{B.2}$$

$$k_f = -0.00013184T + 0.13326, \tag{B.3}$$

$$\mu_f = 10113T^{-1.755}, \tag{B.4}$$

where T is used to indicate temperature [°C], and ρ_f [kg/m^3], $c_{p,f}$ [J/(kg°C)], k_f [W/(m°C)], and μ_f [Ns/m^2] are the density, specific heat, thermal conductivity, and dynamic viscosity of the HTF, respectively.

The density ρ_p [kg/m^3] and the thermal conductivity k_p [W/(m°C)] of the PCM (RigidexHD6070EA) are given by

$$\rho_p = \frac{167.2182}{1.0 + e^{[0.078916(T-129.9861)]}} + 760.8218, \tag{B.5}$$

$$k_p = \frac{0.41857}{1.0 + e^{[0.036647(T-96.162)]}} + 0.15406. \tag{B.6}$$

Relevant parameters of the ice tank are provided in Table B.3.

The thermophysical properties of the HTF (mixture of water–glycol at 34%) are provided in polynomial form as [40]:

$$\rho_f = -1.4205\times10^{-7}T^4 + 3.6616\times10^{-5}T^3 - 0.0038T^2 - 0.3740T + 1.0633\times10^3, \tag{B.7}$$

$$c_{p,f} = -5.9524 \times 10^{-4}T^2 + 2.7976T + 3.5643 \times 10^3, \tag{B.8}$$

$$\mu_f = 2.4811 \times 10^{-10}T^4 - 5.9628 \times 10^{-8}T^3 - 5.166 \times 10^{-6}T^2 - 2.1234 \times 10^{-4}T + 0.0049, \tag{B.9}$$

$$k_f = 2.3674 \times 10^{-11}T^4 - 3.1516 \times 10^{-10}T^3 - 7.8598 \times 10^{-7}T^2 + 1.9683 \times 10^{-4}T + 0.4662, \tag{B.10}$$

$$\mathrm{Pr}_f = 0.0102T^2 - 1.4T + 48.4288, \tag{B.11}$$

where Pr_f is the Prandtl number of the HTF.

Appendix C. Calculation of the overall heat transfer coefficient

This appendix presents a general procedure to calculate the overall heat transfer coefficient U for the 1-D dynamic model of a TES unit and its non-linear observer. The procedure is reproduced from [40] but included here for completeness.

The first step is to calculate the mean velocity v_f [m/s] of the HTF with

$$v_f = \frac{\dot{m}_f}{\rho_f A_c} = \frac{\dot{m}_f}{\rho_f \pi r_i^2}, \tag{C.1}$$

where A_c [m^2] is the cross-section area of the tubes inside the LHTES unit, r_i [m] is the internal radius of the internal tubes of the LHTES unit, $\dot{m}_f$ [kg/s] is the mass flow rate of the HTF and ρ_f [kg/m^3] is the density of the HTF.

The second step is to calculate the Reynolds number Re, given by

$$\mathrm{Re} = \frac{\rho_f v_f D_t}{\mu_f}, \tag{C.2}$$

where D_t [m] is the hydraulic diameter of the tube and μ_f [Ns/m^2] is the dynamic viscosity of the fluid. The value of Re determines whether the fluid is laminar or turbulent. For simplicity, the transition zone between laminar and turbulent flow is not considered. Thus, for laminar flow, it is assumed that the Nusselt number Nu, which is key for calculating the convection heat transfer coefficient, has a constant value of Nu = 4.36. For a turbulent flow, this is defined instead by

$$\mathrm{Nu} = 0.023\mathrm{Re}^{4/5}\mathrm{Pr}^n, \tag{C.3}$$

where Pr is the Prandtl number of the HTF, with $n = 0.4$ for a heating process and $n = 0.3$ for a cooling process. The convection heat transfer coefficient U_{cv} [W/(m^2°C)] of the HTF is calculated by

$$U_{cv} = \frac{\mathrm{Nu}k_f}{D_t}, \tag{C.4}$$

where k_f [W/(m°C)] is the thermal conductivity of the fluid. On the other hand, the conduction heat transfer coefficient in the tube wall $U_{cd,t}$ [W/(m^2°C)] is calculated as

$$U_{cd,t} = \frac{k_t}{\ln(r_o/r_i)\, r_i}, \tag{C.5}$$

where k_f [W/(m°C)] is the thermal conductivity of the tube. The conduction heat transfer coefficient presented in the PCM $U_{cd,p}$ [W/(m^2°C)] is calculated as

$$U_{cd,p} = \frac{k_p}{\ln(r_p/r_o)\, r_i}, \tag{C.6}$$

where k_p [W/(m°C)] is the thermal conductivity of the PCM and r_p is the radius of the control volume of the PCM. Finally, the overall heat transfer coefficient U [W/(m^2°C)] is given by

$$U = \frac{\beta}{U_{cv}^{-1} + U_{cd,t}^{-1} + U_{cd,p}^{-1}}, \tag{C.7}$$

where β is a correction factor. This correction factor is used to reduce the error given by the heat losses presented in an LHTES unit. In [40], β is also used to reduce the error from assuming that the spiralled tubes in the ice tank have been modelled as unrolled tubes.

The previous procedure can be employed to accurately calculate U and, thus, model different TES configurations. Moreover, the calculation of U is done dynamically, so this considers any changes in the operating conditions, such as varying flow rates and temperatures of the HTF.

Appendix D. Derivation of the non-linear observer

The observer structure employed in this work is defined in Eq. (4) within Section 3. For completeness, its implementation for the SoC calculation of the shell and tube TES unit is explained in this section.

The shell and tube TES unit is described by a set of ODEs represented by $f(\mathbf{x},\mathbf{u})$, where $\mathbf{x}$ stands for the states and $\mathbf{u}$ for the inputs of the system. The system states are the temperatures T of the discretised volumes of the HTF and the PCM. The 1-D dynamic model of the shell and tube TES unit is given by [42]

$$\begin{bmatrix} \dot{T}_{f,1} \\ \dot{T}_{p,1} \\ \vdots \\ \dot{T}_{f,i} \\ \dot{T}_{p,i} \\ \vdots \\ \dot{T}_{f,N} \\ \dot{T}_{p,N} \end{bmatrix} = \begin{bmatrix} \frac{\dot{m}_f c_{p,f,1}(T_{f,in}-T_{f,1})+U(A_{tr}/N)(T_{p,1}-T_{f,1})}{\rho_{f,1}c_{p,f,1}(V_f/N)} \\ \frac{U(A_{tr}/N)(T_{f,1}-T_{p,1})}{\rho_{p,1}c_{p,p,1}(V_p/N)} \\ \vdots \\ \frac{\dot{m}_f c_{p,f,i}(T_{f,i-1}-T_i)+U(A_{tr}/N)(T_{p,i}-T_{f,i})}{\rho_{f,i}c_{p,f,i}(V_f/N)} \\ \frac{U(A_{tr}/N)(T_{f,i}-T_{p,i})}{\rho_{p,i}c_{p,p,i}(V_p/N)} \\ \vdots \\ \frac{\dot{m}_f c_{p,f,N-1}(T_{f,N-1}-T_N)+U(A_{tr}/N)(T_{p,N}-T_{f,N})}{\rho_{f,N}c_{p,f,N}(V_f/N)} \\ \frac{U(A_{tr}/N)(T_{f,N}-T_{p,N})}{\rho_{p,N}c_{p,p,N}(V_p/N)} \end{bmatrix}, \tag{D.1}$$

where subscripts 'f' and 'p' stand for the HTF and the PCM.

The use of a state–space representation facilitates the design and implementation of an observer. To adopt a state–space notation, variable T is replaced by x, which denotes a state variable within the state vector $\mathbf{x}$. For the TES unit, the number of nodes is defined by the system discretisation and represented by N. Each node considers two temperatures: T_f and T_p. Each temperature represents a system state, and the number of the system states is $2N$. This way, the state–space representation is given by

$$\begin{bmatrix} \dot{T}_{f,1} \\ \dot{T}_{p,1} \\ \vdots \\ \dot{T}_{f,i} \\ \dot{T}_{p,i} \\ \vdots \\ \dot{T}_{f,N} \\ \dot{T}_{p,N} \end{bmatrix} = \begin{bmatrix} \dot{x}_1 \\ \dot{x}_2 \\ \vdots \\ \dot{x}_k \\ \dot{x}_{k+1} \\ \vdots \\ \dot{x}_{2N-1} \\ \dot{x}_{2N} \end{bmatrix} = \begin{bmatrix} \frac{\dot{m}_f c_{p,f,1}(T_{f,in}-x_1)+U(A_{tr}/N)(x_2-x_1)}{\rho_{f,1}c_{p,f,1}(V_f/N)} \\ \frac{U(A_{tr}/N)(x_1-x_2)}{\rho_{p,2}c_{p,p,2}(V_p/N)} \\ \vdots \\ \frac{\dot{m}_f c_{p,f,k}(x_{k-2}-x_k)+U(A_{tr}/N)(x_{k+1}-x_k)}{\rho_{f,k}c_{p,f,k}(V_f/N)} \\ \frac{U(A_{tr}/N)(x_k-x_{k+1})}{\rho_{p,k+1}c_{p,p,k+1}(V_p/N)} \\ \vdots \\ \frac{\dot{m}_f c_{p,f,N-1}(x_{2N-3}-x_{2N-1})+U(A_{tr}/N)(x_{2N}-x_{2N-1})}{\rho_{f,2N-1}c_{p,f,2N-1}(V_f/N)} \\ \frac{U(A_{tr}/N)(x_{2N-1}-x_{2N})}{\rho_{p,2N}c_{p,p,2N}(V_p/N)} \end{bmatrix}. \tag{D.2}$$

The next step in the design is defining the outputs of the system (within output vector $\mathbf{y}$) that are used to feed the observer. For the shell and tube TES unit, only the output temperature of the HTF is needed. This is incidentally a system state, given by

$$\mathbf{y} = j(x) = T_{f,o} = T_{f,N} = x_{2N-1}. \tag{D.3}$$

Using the structure of the observer in (4) (i.e. $\dot{\hat{\mathbf{x}}} = f(\hat{\mathbf{x}},\mathbf{u}) + \mathbf{J}\left[\mathbf{y} - j(x)\right]$) and replacing the state vector $\mathbf{x}$ by the vector with the estimated states $\hat{\mathbf{x}}$, the observer (8) is obtained.

A similar procedure was followed to develop the observer (12) of the ice TES unit, for which the 1-D dynamic model presented in [40] was adopted.

Appendix E. PDFs for the specific heat–temperature curve of a PCM

The specific heat–temperature curve of the PCM for the dynamic model of the shell and tube TES is described by [41]

$$c_p(T_p) = 1000\left[a_0 + a_1 T_p + b_1 \varphi(T_p)\right], \tag{E.1}$$

and for the ice TES tank model, the specific heat–temperature curve of water is defined as [40]

$$c_{p,w}(T_w) = 1000\left[a_0 + b_1\left(\varphi(T_w) - a_1\right)\right], \tag{E.2}$$

Table E.4
Parameters used in (E.1) and (E.2) to obtain the specific heat–temperature curves of the PCM and water.

	a_0	a_1	b_1	Parameters of φ
c_{p,φ^G}	0.8405	6.5655×10^3	261.55	$\eta = 126.5,\ \theta = 9.3897$
c_{p,φ^W}	5.5623	6.5655×10^3	99.4567	$\eta = 134,\ \gamma = 2.944,\ \theta = 5.6185$
c_{p,φ^L}	2.903	6.5655×10^3	220.0744	$\eta = 126,\ \gamma = 2.118,\ \theta = 4.7951$
$c_{p,w}$ (φ^L)	4.18	0.0128	406.12	$\eta = 0,\ \gamma = 2.118,\ \theta = 0.65$

where a_0, a_1 and b_1 are dimensionless parameters and φ is a PDF.

Three different PDFs are employed to define the specific heat–temperature curve of the PCM for the LHTES units. These functions are dependent of PCM temperature (T). The Gumbel minimum distribution (extreme value type I) is given by

$$\varphi^{\mathrm{G}}(T,\eta,\theta) = \left(\frac{1}{\theta}\right)\exp\left(\frac{T-\eta}{\theta}\right)\exp\left[-\exp\left(\frac{T-\eta}{\theta}\right)\right], \tag{E.3}$$

where η is the location parameter and θ is the scale parameter (both dimensionless).

The adaptation of the Weibull distribution is defined as

$$\varphi^{\mathrm{W}}(T,\gamma,\eta,\theta) = \begin{cases} \frac{\gamma}{\theta}\left(-\frac{T-\eta}{\theta}\right)^{\gamma-1}\exp\left[\left(\frac{T-\eta}{\theta}\right)^{\gamma}\right] & T < \eta \\ 0, & T \geq \eta \end{cases}, \tag{E.4}$$

where γ is the shape parameter, η is the location parameter and θ is the scale parameter (all dimensionless).

The adaptation of the Lognormal distribution is described by

$$\varphi^{\mathrm{L}}(T,\gamma,\eta,\theta) = \begin{cases} \frac{\exp\left[-\left((\ln[-(T-\eta)/\theta])^2/(2\gamma^2)\right)\right]}{-(T-\eta)\gamma\sqrt{2\pi}}, & T < \eta \\ 0, & T \geq \eta \end{cases}, \tag{E.5}$$

where γ is the shape parameter, η is the location parameter and θ is the scale parameter (all dimensionless).

The parameter values for the specific heat–temperature curves employed in this work are given in Table E.4.

References

[1] Tahiri A, Smith KM, Thorsen JE, Hviid CA, Svendsen S. Staged control of domestic hot water storage tanks to support district heating efficiency. Energy 2023;263:125493. http://dx.doi.org/10.1016/j.energy.2022.125493.

[2] District heating and cooling systems | ENGIE. 2022, https://www.engie.com/en/businesses/district-heating-cooling-systems/. [Accessed 20 October 2022].

[3] Lyu W, Wang Z, Li X, Deng G, Xu Z, Li H, et al. Influence of the water tank size and air source heat pump size on the energy saving potential of the energy storage heating system. J Energy Storage 2022;55:105542. http://dx.doi.org/10.1016/j.est.2022.105542.

[4] Zhou D, Zhao CY, Tian Y. Review on thermal energy storage with phase change materials (PCMs) in building applications. Appl Energy 2012;92:593–605. http://dx.doi.org/10.1016/j.apenergy.2011.08.025.

[5] Pachori H, Choudhary T, Sheorey T. Significance of thermal energy storage material in solar air heaters. Mater Today: Proc 2022;56:126–34. http://dx.doi.org/10.1016/j.matpr.2021.12.516.

[6] Fan Y, Zhang C, Jiang L, Zhang X, Qiu L. Exploration on two-stage latent thermal energy storage for heat recovery in cryogenic air separation purification system. Energy 2022;239:122111. http://dx.doi.org/10.1016/j.energy.2021.122111.

[7] Sharif MKA, Al-Abidi AA, Mat S, Sopian K, Ruslan MH, Sulaiman MY, et al. Review of the application of phase change material for heating and domestic hot water systems. Renew Sustain Energy Rev 2015;42:557–68. http://dx.doi.org/10.1016/j.rser.2014.09.034.

[8] Lund PD, Lindgren J, Mikkola J, Salpakari J. Review of energy system flexibility measures to enable high levels of variable renewable electricity. Renew Sustain Energy Rev 2015;45:785–807. http://dx.doi.org/10.1016/j.rser.2015.01.057.

[9] Siddiqui S, Macadam J, Barrett M. The operation of district heating with heat pumps and thermal energy storage in a zero-emission scenario. Energy Rep 2021;7:176–83. http://dx.doi.org/10.1016/j.egyr.2021.08.157.

[10] Xu T, Humire EN, Chiu JN, Sawalha S. Latent heat storage integration into heat pump based heating systems for energy-efficient load shifting. Energy Convers Manage 2021;236:114042. http://dx.doi.org/10.1016/j.enconman.2021.114042.

[11] Liu B, Zhang X, Ji J. Review on solar collector systems integrated with phase-change material thermal storage technology and their residential applications. Int J Energy Res 2021;45(6):8347–69. http://dx.doi.org/10.1002/er.6397.

[12] Palacios A, Barreneche C, Navarro ME, Ding Y. Thermal energy storage technologies for concentrated solar power – A review from a materials perspective. Renew Energy 2020;156:1244–65. http://dx.doi.org/10.1016/j.renene.2019.10.127.

[13] Airò Farulla G, Cellura M, Guarino F, Ferraro M. A review of thermochemical energy storage systems for power grid support. Appl Sci 2020;10(9):3142. http://dx.doi.org/10.3390/app10093142.

[14] Heier J, Bales C, Martin V. Combining thermal energy storage with buildings – A review. Renew Sustain Energy Rev 2015;42:1305–25. http://dx.doi.org/10.1016/j.rser.2014.11.031.

[15] Carpaneto E, Lazzeroni P, Repetto M. Optimal integration of solar energy in a district heating network. Renew Energy 2015;75:714–21. http://dx.doi.org/10.1016/j.renene.2014.10.055.

[16] Zsembinszki G, Fernández C, Vérez D, Cabeza LF. Deep learning optimal control for a complex hybrid energy storage system. Buildings 2021;11(5). http://dx.doi.org/10.3390/buildings11050194.

[17] Cupelli L, Schumacher M, Monti A, Mueller D, De Tommasi L, Kouramas K. Chapter four - simulation tools and optimization algorithms for efficient energy management in neighborhoods. In: Energy positive neighborhoods and smart energy districts. Academic Press; 2017, p. 57–100. http://dx.doi.org/10.1016/B978-0-12-809951-3.00004-1.

[18] Tarragona J, Fernández C, de Gracia A. Model predictive control applied to a heating system with PV panels and thermal energy storage. Energy 2020;197:117229. http://dx.doi.org/10.1016/j.energy.2020.117229.

[19] Thieblemont H, Haghighat F, Ooka R, Moreau A. Predictive control strategies based on weather forecast in buildings with energy storage system: A review of the state-of-the art. Energy Build 2017;153:485–500. http://dx.doi.org/10.1016/j.enbuild.2017.08.010.

[20] Morales Sandoval DA, De La Cruz Loredo I, Bastida H, Badman JJR, Ugalde-Loo CE. Design and verification of an effective state-of-charge estimator for thermal energy storage. IET Smart Grid 2021;4(2):202–14. http://dx.doi.org/10.1049/stg2.12024.

[21] Dinçer I, Rosen MA. Thermal energy storage: Systems and applications. John Wiley & Sons; 2011.

[22] Lizana J, Chacartegui R, Barrios-Padura A, Valverde JM. Advances in thermal energy storage materials and their applications towards zero energy buildings: A critical review. Appl Energy 2017;203:219–39. http://dx.doi.org/10.1016/j.apenergy.2017.06.008.

[23] Domanski R, El-Sebaii AA, Jaworski M. Cooking during off-sunshine hours using PCMs as storage media. Energy 1995;20(7):607–16. http://dx.doi.org/10.1016/0360-5442(95)00012-6.

[24] Liu G, Li Q, Wu J, Xie R, Zou Y, Marson A, et al. Improving system performance of the refrigeration unit using phase change material (PCM) for transport refrigerated vehicles: An experimental investigation in South China. J Energy Storage 2022;51:104435. http://dx.doi.org/10.1016/j.est.2022.104435.

[25] Athienitis AK, Liu C, Hawes D, Banu D, Feldman D. Investigation of the thermal performance of a passive solar test-room with wall latent heat storage. Build Environ 1997;32(5):405–10. http://dx.doi.org/10.1016/S0360-1323(97)00009-7.

[26] Cabeza LF, Castellón C, Nogués M, Medrano M, Leppers R, Zubillaga O. Use of microencapsulated PCM in concrete walls for energy savings. Energy Build 2007;39(2):113–9. http://dx.doi.org/10.1016/j.enbuild.2006.03.030.

[27] Koschenz M, Lehmann B. Development of a thermally activated ceiling panel with PCM for application in lightweight and retrofitted buildings. Energy Build 2004;36(6):567–78. http://dx.doi.org/10.1016/j.enbuild.2004.01.029.

[28] Sharma A, Tyagi VV, Chen CR, Buddhi D. Review on thermal energy storage with phase change materials and applications. Renew Sustain Energy Rev 2009;13(2):318–45. http://dx.doi.org/10.1016/j.rser.2007.10.005.

[29] Bruno F, Belusko M, Liu M, Tay NHS. 9 - Using solid-liquid phase change materials (PCMs) in thermal energy storage systems. In: Cabeza LF, editor. Advances in thermal energy storage systems. Woodhead publishing series in energy, Woodhead Publishing; 2015, p. 201–46. http://dx.doi.org/10.1533/9781782420965.2.201.

[30] Shete KP, de Bruyn Kops SM, Kosanovic DB. A first principles framework to predict the transient performance of latent heat thermal energy storage. J Energy Storage 2021;36:102388. http://dx.doi.org/10.1016/j.est.2021.102388.

[31] Zsembinszki G, Orozco C, Gasia J, Barz T, Emhofer J, Cabeza LF. Evaluation of the state of charge of a solid/liquid phase change material in a thermal energy storage tank. Energies 2020;13(6):1425. http://dx.doi.org/10.3390/en13061425.

[32] Steinmaurer G, Krupa M, Kefer P. Development of sensors for measuring the enthalpy of PCM storage systems. Energy Procedia 2014;48:440–6. http://dx.doi.org/10.1016/j.egypro.2014.02.052.

[33] Stovall TK. Calmac ice storage test report. Tech. rep. ORNL/TM-11582, Oak Ridge National Lab., TN (United States); 1991, http://dx.doi.org/10.2172/5210651, https://www.osti.gov/biblio/5210651.

[34] Kreuzinger T, Bitzer M, Marquardt W. State estimation of a stratified storage tank. Control Eng Pract 2008;16(3):308–20. http://dx.doi.org/10.1016/j.conengprac.2007.04.013.

[35] Barz T, Seliger D, Marx K, Sommer A, Walter SF, Bock HG, et al. State and state of charge estimation for a latent heat storage. Control Eng Pract 2018;72:151–66. http://dx.doi.org/10.1016/j.conengprac.2017.11.006.

[36] Khalil H. Nonlinear control: Global edition. 1st ed.. Essex, England: Pearson; 2015.

[37] Khan ZA, Shrivastava P, Amrr SM, Mekhilef S, Algethami AA, Seyedmahmoudian M, et al. A comparative study on different online state of charge estimation algorithms for lithium-ion batteries. Sustainability 2022;14(12):7412. http://dx.doi.org/10.3390/su14127412.

[38] Polóni T, Figueroa-Santos MA, Siegel JB, Stefanopoulou AG. Integration of non-monotonic cell swelling characteristic for state-of-charge estimation. In: 2018 Annual American control conference. 2018, http://dx.doi.org/10.23919/ACC.2018.8431237.

[39] Hernández E, Prieur C, Cerpa E. A tracking problem for the state of charge in an electrochemical Li-ion battery model. Math Control Related Fields 2022;12(3):709–32. http://dx.doi.org/10.3934/mcrf.2021041.

[40] Bastida H, Ugalde-Loo CE, Abeysekera M, Jenkins N. Dynamic modelling of ice-based thermal energy storage for cooling applications. IET Energy Syst Integr 2022;4(3). http://dx.doi.org/10.1049/esi2.12061.

[41] Barz T, Zauner C, Lager D, López Cárdenas DC, Hengstberger F, Cruz Bournazou MN, et al. Experimental analysis and numerical modeling of a shell and tube heat storage unit with phase change materials. Ind Eng Chem Res 2016;55(29):8154–64. http://dx.doi.org/10.1021/acs.iecr.6b01080.

[42] Bastida H, De la Cruz-Loredo I, Ugalde-Loo CE. Effective One-Dimensional Dynamic Modelling of Latent Heat Thermal Energy Storage Units for Heating Applications. Unpublished results.

[43] Pernsteiner D, Schirrer A, Kasper L, Hofmann R, Jakubek S. State estimation concept for a nonlinear melting/solidification problem of a latent heat thermal energy storage. Comput Chem Eng 2021;153:107444. http://dx.doi.org/10.1016/j.compchemeng.2021.107444.

[44] Ghasemi K, Tasnim S, Mahmud S. PCM, nano/microencapsulation and slurries: A review of fundamentals, categories, fabrication, numerical models and applications. Sustain Energy Technol Assess 2022;52:102084. http://dx.doi.org/10.1016/j.seta.2022.102084.

[45] Rigidex HD6070EA data sheet. 2022, https://www.ineos.com/shop-document/?grade=HD6070EA&bu=INEOS+O+%2526+P+Europe&documentType=TechnicalData+Sheet&docLanguage=EN&version=2566d5566193b465bb3681d8abe64fea. [Accessed 6 November 2022].

[46] López-Navarro A, Biosca-Taronger J, Torregrosa-Jaime B, Corberán JM, Bote-García JL, Payá J. Experimental investigations on the influence of ice floating in an internal melt ice-on-coil tank. Energy Build 2013;57:20–5. http://dx.doi.org/10.1016/j.enbuild.2012.10.040.

[47] López-Navarro A, Biosca-Taronger J, Torregrosa-Jaime B, Martínez-Galván I, Corberán JM, Esteban-Matías JC, et al. Experimental investigation of the temperatures and performance of a commercial ice-storage tank. Int J Refrig 2013;36(4):1310–8. http://dx.doi.org/10.1016/j.ijrefrig.2012.09.008.

[48] Drees KH, Braun JE. Modeling of area-constrained ice storage tanks. HVAC R Res 1995;1(2):143–58. http://dx.doi.org/10.1080/10789669.1995.10391315.

[49] Marlotherm SH heat transfer fluid by Eastman. 2022, https://marlotherm.nl/en/products/marlotherm-sh/. [Accessed 10 October 2022].

[50] Diaconu BM, Varga S, Oliveira AC. Experimental assessment of heat storage properties and heat transfer characteristics of a phase change material slurry for air conditioning applications. Appl Energy 2010;87(2):620–8. http://dx.doi.org/10.1016/j.apenergy.2009.05.002.

[51] Musavi SM, Roudini G, Barahuie F, Masuri SUB. Thermal energy storage property and temperature control performance of phase change materials eutectic mixture nanocomposite. Micro Nanosyst 13. http://dx.doi.org/10.2174/1876402913666210903162938.

[52] CALMAC - ice bank energy storage tanks. CALMAC, NJ. 2022, https://www.calmac.com/. [Accessed 03 October 2022].

[53] Industrial chemicals | Industrial specialites'. 2022, https://www.crodaindustrialspecialties.com/. [Accessed 20 October 2022].

[54] Homepage | Sunamp | Global | World leading thermal storage technologies. 2022, https://www.sunamp.com/. [Accessed 20 October 2022].

[55] Hu H, Jin X, Zhang X. Effect of supercooling on the solidification process of the phase change material. Energy Procedia 2017;105:4321–7. http://dx.doi.org/10.1016/j.egypro.2017.03.905.

[56] Incropera FP, et al. Principles of heat and mass transfer. 7th ed.. New York: Wiley & Sons; 2013.